

A Catalog of Broad Absorption Line Quasars from the Sloan Digital Sky Survey Third Data Release

Jonathan R. Trump,^{1,2} Patrick B. Hall,^{3,4} Timothy A. Reichard,⁵ Gordon T. Richards,^{3,5}
 Donald P. Schneider,¹ Daniel E. Vanden Berk,¹ Gillian R. Knapp,³ Scott F. Anderson,⁶
 Xiaohui Fan,² J. Brinkman,⁷ S. J. Kleinman,⁸ and Atsuko Nitta⁸

ABSTRACT

We present a total of 4784 unique broad absorption line quasars from the Sloan Digital Sky Survey Third Data Release. An automated algorithm was used to match a continuum to each quasar and to identify regions of flux at least 10% below the continuum over a velocity range of at least 1000 km s⁻¹ in the CIV and MgII absorption regions. The model continuum was selected as the best-fit match from a set of template quasar spectra binned in luminosity, emission line width, and redshift, with the power-law spectral index and amount of dust reddening as additional free parameters. We characterize our sample through the traditional “balnicity” index and a revised absorption index, as well as through parameters such as the width, outflow velocity, fractional depth and number of troughs. From a sample of 16883 quasars at $1.7 \leq z \leq 4.38$, we identify 4386 (26.0%) quasars with broad CIV absorption, of which 1756 (10.4%) satisfy traditional selection criteria. From a sample of 34973 quasars at $0.5 \leq z \leq 2.15$, we identify 457 (1.31%) quasars with broad MgII absorption, 191 (0.55%) of which satisfy traditional selection criteria. We also provide a supplementary list of 39 visually identified $z > 4.38$ quasars with broad CIV absorption. We find

¹Department of Astronomy and Astrophysics, The Pennsylvania State University, University Park, PA 16802.

²Steward Observatory, University of Arizona, 933 North Cherry Avenue, Tucson, AZ 85721

³Princeton University Observatory, Princeton, NJ 08544.

⁴Department of Physics & Astronomy, York University, 4700 Keele Street, Toronto, Ontario, M3J 1P3, Canada

⁵The Johns Hopkins University, 3400 North Charles Street, Baltimore, MD 21218-2686

⁶Department of Astronomy, University of Washington, Box 351580, Seattle, WA 98195

⁷Apache Point Observatory, P.O. Box 59, Sunspot, NM 88349-0059.

⁸Subaru Telescope, 650 N A’ohoku Pl., Hilo, HI 96720

that broad absorption line quasars may have broader emission lines on average than other quasars.

Subject headings: galaxies: active — quasars: general — quasars: absorption lines — quasars: emission lines — catalogs

1. Introduction

The nature of intrinsic absorption in quasars and other active galactic nuclei (AGN) has important implications for physical models of the quasar “central engine.” The subclass of broad absorption line quasars (BALQSOs) is thought to account for between 10% and 30% of quasars. The exact fraction of BALQSOs is nontrivial to determine because of differential selection effects between BALQSO and non-BALQSOs. Hewett & Foltz (2003) report a corrected BALQSO fraction of $22 \pm 4\%$ for their sample of 42 bright ($B_J < 19$) quasars, Tolea, Krolik & Tsvetanov (2002) estimate a fraction of $\sim 15\%$ from their sample of 116 quasars, and Reichard et al. (2003b) estimate a corrected fraction of $15.9 \pm 1.4\%$ for a sample of 224 quasars with $i \lesssim 20$.

Broad absorption troughs are caused by gas outflowing at high velocities from quasars. It has been suggested that some or all BALQSOs may be a unique class of quasars (Surdej & Hutsemekers 1987), perhaps in a different stage of their life cycle (Hazard et al. 1984, Boroson & Meyers 1992, Becker et al. 2000). Other authors suggest the differences from “standard” quasars arise because BALQSOs are observed at a different orientation (Weymann et al. 1991; Ogle et al. 1999; Schmidt & Hines 1999; Hall et al. 2002). BALQSOs generally have UV to soft X-ray flux ratios 10-30 times smaller than unabsorbed quasars (Brandt, Laor, & Wills 2000), though if BALQSOs are corrected for intrinsic absorption, their UV to soft X-ray flux ratio is typical of normal quasars (Gallagher et al. 2002).

Three sources of material can cause absorption in the spectrum of a quasar: (1) “intrinsic,” produced by processes related to the AGN itself, (2) “host,” produced by material in the quasar’s host galaxy unrelated to the AGN, and (3) “intervening,” absorbing material along the line of sight but not physically related to the AGN or host galaxy. Broader and higher-velocity absorption troughs are more likely to be intrinsic, since only the AGN can feasibly accelerate matter to the velocities and velocity widths observed in BALQSOs (both often $\geq 10000 \text{ km s}^{-1}$).

BALQSOs are classified into three subcategories based upon the material producing the BAL troughs. High-ionization BALQSOs (HiBALs) contain strong, broad absorption troughs shortward of high-ionization emission lines and are typically identified through the

presence of C IV absorption troughs. Low-ionization BALQSOs (LoBALs) contain HiBAL features but also have absorption from low-ionization lines such as Mg II. LoBALs with excited-state Fe II or Fe III absorption are called FeLoBALs.

The first large sample of BALQSOs was analyzed by Weymann et al. (1991), who defined BALQSOs as quasars exhibiting C IV absorption troughs broader than 2000 km s^{-1} . This minimum trough width was defined primarily to avoid contamination by noise, but also to reject multiple overlapping intervening systems. We call these objects “traditional” BALQSOs; they are fully defined in §4.1. Reichard et al. (2003a) expanded the number of known traditional BALQSOs with a catalog of 224 BALQSOs selected from the Sloan Digital Sky Survey (SDSS; York et al. 2000) Early Data Release (EDR; Stoughton et al. 2002a) quasar catalog (Schneider et al. 2002). (See Menou et al. (2001) and Tolea, Krolik & Tsvetanov (2002) for earlier SDSS work on BALQSOs.)

In this paper we present a catalog of 4784 BALQSOs from the SDSS Third Data Release (DR3; Abazajian et al. 2005). Our catalog represents a substantial increase in the number of known BALQSOs primarily because the SDSS DR3 is more than ten times larger than the SDSS EDR. We retain the traditional BALQSO definition as all quasars with “balnicity index” $BI > 0$ (Weymann et al. 1991, also defined in §4.1), but also extend our analysis of the intrinsic absorption lines in quasars to include absorption troughs broader than 1000 km s^{-1} regardless of their velocity shift from the quasar redshift. Our full definition of BALQSOs is given in §4.3. Our automated algorithms identify HiBALs via C IV from $1.7 \leq z \leq 4.38$ and LoBALs via Mg II from $0.5 \leq z \leq 2.15$. These redshift constraints are set by the wavelength coverage of the SDSS spectra (3800–9200 Å). FeLoBAL objects can have strong absorption throughout their spectra because there are lots of Fe lines in several ionization states. FeLoBALs are easily identified through visual inspection of HiBALs and LoBALs, but are very difficult to fit with a continuum in the automated methods.

The parent sample for our catalog is discussed in §2. In §3 we describe the automated BALQSO identification scheme and motivate the expansion of the BALQSO definition. We define the metrics used to describe both the traditional BALQSOs and the BALQSOs of the catalog in §4. The different objects included in the catalog are discussed in §5. We suggest some of the implications of our statistical sample of BALQSOs in §6, though a more complete analysis of the sample will be presented by Hall et al. (2006). Throughout this paper, we adopt a cosmology consistent with WMAP results of $h = 0.70$, $\Omega_M = 0.3$, $\Omega_\Lambda = 0.7$ (Spergel et al. 2003).

2. Observations: The Sloan Digital Sky Survey

The parent sample for the BALQSO catalog is the SDSS DR3 quasar catalog (Schneider et al. 2005). The SDSS is a wide-field survey operated by the Astrophysical Research Consortium on a 2.5 m telescope (Gunn et al. 2006) at the Apache Point Observatory, New Mexico. All images are taken in the five bands u , g , r , i , z (Fukugita et al. 1996) by the CCD camera (Gunn et al. 1998). SDSS magnitudes are expressed in the asinh magnitude system (Lupton, Gunn, & Szalay 1999). Calibration of the photometry is described by Hogg et al. (2001), Smith et al. (2002), and Tucker et al. (2006), photometric processing by Lupton et al. (2001), and the photometric quality assesement by Ivezić et al. (2004). Quasar candidates are selected for spectroscopic targeting based on the selection algorithm of Richards et al. (2002). Spectroscopy of all objects in the DR3 was acquired via 826 3° diameter plates with 640 drilled fibers per plate, with the plates tiled onto the sky using the algorithm of Blanton et al. (2003). The spectroscopic pipeline is discussed by Stoughton et al. (2002a). The resolution of the SDSS spectra is 1800–2100 over most of the wavelength coverage, 3800-9200 Å.

The SDSS DR3 quasar catalog contains all 46420 spectroscopically identified quasars in the DR3 with $M_i < -22$. We correct all spectra for the Galactic extinction given in the maps of Schlegel, Finkbeiner, & Davis (1998) using the empirical selective extinction function of Cardelli, Clayton, & Mathis (1989). We boxcar smooth all spectra by ~ 3 pixels (roughly the resolution) to reduce noise and prevent the use of unresolved (spurious) features. The SDSS spectroscopic pipeline automatically interpolates over bad pixels, although on either side of an interpolated region there are typically a few pixels with a very low signal-to-noise ratio. To correct this we extend both sides of all pipeline-interpolated regions by three pixels and ignore the entire extended interpolated regions. Our analyses are limited to SDSS spectra in which the both the region up to 29000 km s $^{-1}$ shortward of the MgII or CIV emission line and the normalization region (2910 ± 10 Å for MgII and 1710 ± 10 Å for CIV) are redshifted into the observed spectral range. Thus we searched for MgII BALQSOs among 34973 objects with $0.5 \leq z \leq 2.15$ and CIV BALQSOs among 16883 objects with $1.7 \leq z \leq 4.38$.

3. Construction of the Catalog

The need for objective selection and quantification of BALQSOs and traditional BALQSOs in our large data set necessitated the use of an automatic selection algorithm. Our basic approach was that of Reichard et al. (2003a): a continuum fit was made to each quasar spectrum and absorption features were identified as dips in the spectrum below the continuum. But whereas Reichard et al. (2003a) used a single template spectrum to fit each sample con-

tinuum, we employ a best-fit template from a set of template spectra binned in line width, luminosity, and redshift. We also extend the fitting ranges from those of Reichard et al. (2003a) to better account for line shapes by including emission line profiles redward of the center wavelength (where absorption should not play a significant role). We also independently scale the C IV and Mg II emission line regions of the best-fit template. The template spectra are described in detail in §3.1 and the fitting process in §3.2.

3.1. Template Spectra

Most quasars have broadly similar ultraviolet/optical spectra (e.g., Richards et al. 2001, Vanden Berk et al. 2001), but there are several basic trends which lead to considerable variation among quasar spectra (Marziani et al. 2003). One of the most prominent is the Baldwin (1977) Effect, the well-known anticorrelation between the luminosity of a quasar and the equivalent widths of its emission lines (see also Osmer, Porter, & Green 1994). In addition, Richards et al. (2002) suggested that there may be a relationship between the line shape, equivalent width, and blueshift of the high-ionization (e.g., C IV) lines with respect to the low-ionization (e.g., Mg II) lines of the quasar. Vanden Berk et al. (2003) confirmed the findings of Richards et al. (2002), and also noted that the Baldwin Effect appears to evolve with redshift.

Our fitting process is designed to take advantage of the general similarity of quasar UV/optical spectra with a general first-pass fit, while accounting for the differences arising from line shape, luminosity, high-ionization line blueshift, and redshift. We begin by fitting to a geometric mean composite spectrum constructed using the methods of Vanden Berk et al. (2001) from the quasars in the SDSS First Data Release (DR1; Abazajian et al. 2003) quasar catalog (Schneider et al. 2003). This general first-pass fit is designed to provide initial estimates of spectral index and reddening and to weight out absorption regions from the final fitting process (see §3.2 below). We account for differing luminosities, line widths (and thus indirectly any mean blueshift of C IV with respect to Mg II) and possible redshift trends by finding the best-fit template for each quasar from a set of templates binned in line width, luminosity, and redshift.

Quasars for the set of template spectra were selected from the SpecPhotoAll table of the public DR3 Catalog Archive Server (Stoughton et al. 2002b), requiring a redshift confidence of 95% or greater and rejecting inconsistent or manually corrected redshifts⁹. We

⁹Inconsistent or manually corrected redshifts are rejected by requiring `zStatus` in `{3,4,6,7,9}` in the public SDSS DR3 Catalog Archive Server.

also required either the CIV or MgII line to have been successfully measured by the automated Gaussian-fitting pipeline, with $\chi^2_\nu < 2$, $\text{EW}/\sigma_{\text{EW}} > 10$ and $\text{FWHM}/\sigma_{\text{FWHM}} > 5$. Objects with a null or negative *i*-band magnitude measurement which prevented calculation of the *i*-band absolute magnitude were excluded. Finally, objects with known BALs and strong narrow absorption systems (as identified by various SDSS workers during visual inspections) were excluded to ensure that each template reflected an unabsorbed quasar spectrum.

The properties of the final-fit template samples are shown in Table 1. Composites for CIV were constructed in three redshift ranges: $1.52 < z < 1.9$, $1.9 < z < 2.3$ and $2.3 < z < 4.90$. Within each redshift range, quasars were separated into the upper and lower halves of the absolute *i*-band luminosity distribution. These absolute magnitude bins were further subdivided into quartiles of CIV line width (narrowest, narrow, broad, and broadest). Thus, eight templates were created for each of the three redshift bins. The templates are enumerated in our discussion and final catalog as templates 0-3 representing the less luminous M_i bin in order of narrowest line width to broadest, and templates 4-7 representing the more luminous M_i bin in the same order of line width. An identical approach was used to create MgII templates in the three redshift ranges $0.39 < z < 0.9$, $0.9 < z < 1.4$ and $1.4 < z < 2.2$. Quasars with redshift $1.7 \leq z \leq 2.15$ have two best-fitting templates, one for CIV and one for MgII. The template spectra for CIV are shown in Figure 1 and those for MgII in Figure 2.

3.2. Fitting the Continuum

The ultraviolet/optical continua of quasars are generally well-described by a power-law $f_\nu \propto \nu^{\alpha_\nu}$, where α_ν is the spectral index (e.g, Richstone & Schmidt 1980; Vanden Berk et al. 2001). However, a significant fraction of quasars show evidence of dust reddening (e.g, Richards et al. 2003, Hopkins et al. 2004), which must be included in any automated continuum fitting procedure. For simplicity we assume that all dust reddening beyond the Milky Way value occurs at the quasar redshift. Our automated fitting algorithm works in wavelength space and allows both the spectral index and reddening to vary, using Newton-Raphson minimization to fit the template to each sample spectrum.

The reddening can be described by the dust extinction A_λ ,

$$A_\lambda = E(\lambda - V) + R_V \times E(B - V). \quad (1)$$

Here $E(B - V)$ is the color excess and we adopt $R_V = 2.93$ (as in Pei 1992). In general, dust extinction laws are roughly proportional to λ^{-1} , but there are differences in the exact slope of the extinction and in the strength of the “2175 Å bump” (Sprayberry & Foltz 1992).

Extragalactic sources have a weak or missing 2175 Å bump, so we use the Small Magellanic Cloud reddening law of Prevot et al. (1984) as implemented by Pei (1992).

Each template spectrum $f_{t,\lambda}$ (with intrinsic spectral index $\alpha_{\lambda t}$ and reddening E_t) is fit by adjusting the spectral index α_λ and reddening $E \equiv E(B - V)$ to obtain the fitted template spectrum $f_{t',\lambda}$:

$$f_{t',\lambda}(\alpha_\lambda, E) = f_{t,\lambda} \lambda^{\alpha_\lambda - \alpha_{\lambda t}} 10^{-a(E - E_t)\xi(\lambda)}. \quad (2)$$

where $a = 0.4(1 + R_V)$, $R_V = 2.93$, $\xi(\lambda)$ is the extinction curve, and $\alpha_\lambda \equiv -2 - \alpha_\nu$ is the spectral index. The best-fit template is found by minimizing the chi-squared function

$$\chi^2(\alpha_\lambda, E) = \frac{\sum_\lambda \left[\frac{f_{t',\lambda}(\alpha_\lambda, E) - f_i(\lambda)}{\sigma_i(\lambda)} \right]^2 w(\lambda)}{\sum_\lambda w(\lambda)} \quad (3)$$

where the input spectrum is $f_i(\lambda)$, its error is $\sigma_i(\lambda)$, and $w(\lambda)$ is our weighting function.

Our weighting function $w(\lambda)$ is designed to limit the influence of interpolated pixels, emission line regions, and absorption regions. Interpolated pixels are identified by the error of zero assigned by the pipeline and are given a weight $w(\lambda) = 0$. Weighting the emission line regions and absorption regions is more complicated; see Table 2. Unweighted line regions include the Ly α forest, wavelengths redward of 4050 Å (a single power-law continuum is not a good fit past 4100 Å; see Figure 6 of Vanden Berk et al. 2001), the narrow emission lines [NeV], [OII], and [NeIII], and the blue halves of the NV, SiIV/OIV and CIII] emission lines. Because the widths of the emission lines are important in template selection, $w(\lambda) = 0.5$ is assigned to the red halves of strong emission lines, where intrinsic absorption should not significantly affect the emission profile. Accurately fitting the CIV and MgII emission regions is especially important, so we set $w(\lambda) = 0.5$ within $\pm 5000 \text{ km s}^{-1}$ of the emission line and weight out absorption separately (see below).

Absorption regions in a sample spectrum cause the flux density in the fitted template to be under-estimated. To eliminate these regions from the fitting, we identify absorption from the first-pass fit and then weight out those regions in the final, multiple-template fitting. We identify absorption only from -5000 km s^{-1} to 29000 km s^{-1} relative to the rest wavelengths of the CIV and MgII emission lines.¹⁰ Since poor fits to an emission line can masquerade as absorption troughs, and since our first-pass fit to the spectrum does not fit the emission line shapes, within $\pm 5000 \text{ km s}^{-1}$ of the CIV and MgII rest wavelengths we identify absorption

¹⁰For some quasars, we adjusted the redshift used for the template fitting from the value given in the DR3 quasar catalog to better reflect the redshift of the CIV or MgII line. This is necessary because individual emission lines in quasars can have large velocity shifts relative to the mean emission-line redshift.

relative to a simple linear continuum. Flux density values $\geq 2\sigma$ below this linear continuum, or $\geq 4\sigma$ below the continuum in the region 5000 km s^{-1} to 29000 km s^{-1} shortward of C IV or Mg II, are assigned $w(\lambda) = 0$. Because the C IV and Si IV absorption regions often exhibit similar absorption features, we apply the C IV absorption weighting to the same velocities in the Si IV region (-5000 km s^{-1} to 29000 km s^{-1} from 1402 \AA). The first-pass fit also provides an initial guess on the values of α_λ and E for the multiple-template fitting.

As the values of α_λ and E are varied, the template spectrum is scaled to the quasar spectrum before the χ^2 function is computed. Scaling is performed by calculating the average flux density of each spectrum over small normalization windows. For C IV this window is $1710 \pm 10 \text{ \AA}$, a reasonable continuum region (Vanden Berk et al. 2001). For Mg II BAL identification we use the window $2910 \pm 10 \text{ \AA}$, the first minimum in the Fe II flux redward of Mg II (Vestergaard & Wilkes 2001). A normalization window around 3020 \AA might be better (Sigut, Pradhan, & Nahar 2004), but would limit the LoBAL sample to lower redshifts. We choose this region over the two separate normalization regions of Reichard et al. (2003a) for self-consistency.

The χ^2 function in Equation 3 is minimized using the quadratically converging modified Newton-Raphson method used by Reichard et al. (2003a). The initial values of the spectral index and reddening are from the DR1 quasar composite spectrum: $E = 0$ and $\alpha_\lambda = -1.55$ (corresponding to $\alpha_\nu = -0.45$). The first-pass quasar template spectrum described above is then fit to each quasar spectrum, and the best values of α_λ and E from this fit are used as the initial spectral index and reddening for each template fit. If the Newton-Raphson method does not converge in 50 iterations, the χ^2 function is evaluated over a wide grid of (α_λ, E) to find the minimizing values. This occurred for only 4 C IV and 49 Mg II objects. The grid method is computationally intensive and was used only as a back-up approach.

Because the absorption index starts at the zero velocity shift from the emission line peak, the emission lines of the quasar spectra need to be fit well for an accurate measure of the absorption index. We employ independent emission line scaling for C IV and Mg II, which is justified because we are not seeking a physical characterization of the quasar spectrum in the fitting process, merely a representative continuum with which to identify absorption troughs. After the power-law and reddening fit and the continuum scaling, a linear continuum is subtracted from both emission regions ($1494\text{--}1620 \text{ \AA}$ for C IV and $2686\text{--}2913 \text{ \AA}$ for Mg II). For both lines the template emission line profile is scaled to match the peak flux in the 5-pixel-smoothed sample emission region and the continuum is then re-added to the scaled emission line profile.

Despite our best efforts at automating our template-fitting methods, some objects are poorly fit by all of the templates. A bad template fit often results in a falsely identified or

missed BALQSO. We inspect all quasars in our sample and manually tweak our templates to fit in the CIV or MgII regions where the fitting fails spectacularly and results in a mis-identification. We had to manually fit the template for 347 quasars in the CIV region and 3 in the MgII region. (There are 20 times more CIV BALs than MgII BALs in the catalog, so we would have expected 17 MgII BALs needing adjustment. The difference may be because the spectral region about MgII is easier to fit than the region about CIV.)

4. Selection Criteria of BALQSOs and Traditional BALQSOs

The biggest challenges in identifying intrinsic absorption in quasars are avoiding intervening and host systems and accounting for noise. Completely eliminating host and intervening absorption is impossible without high-resolution spectra, but most systems of this type can be eliminated by defining a minimum width for absorption to be considered an intrinsic trough. To avoid contamination by noise, we must define a minimum depth. We now examine the historical treatment of this issue, and suggest a modified classification system appropriate for the SDSS.

4.1. The Traditional Balnicity Index

Weymann et al. (1991) defined BALs to be at least 2000 km s^{-1} wide and at least 10% below the continuum at maximum depth. These objects were quantified by the “balnicity index” (BI), a sum of the “modified equivalent width” of the portions of all contiguous BAL troughs between 3000 km s^{-1} and 25000 km s^{-1} shortward of 1549 \AA . The equivalent width is “modified” because only those parts of the troughs beyond the first 2000 km s^{-1} of width that dip below 10% of the continuum are included. This is defined:

$$\text{BI} = \int_{3000}^{25000} \left[1 - \frac{f(v)}{0.9} \right] C \, dv \quad (4)$$

where $f(v)$ is the normalized flux, $C = 1$ at trough velocities more than 2000 km s^{-1} from the start of a contiguous trough, and $C = 0$ elsewhere. The BI can take on any value in the range $0 \leq \text{BI} \leq 20000 \text{ km s}^{-1}$. The formal error on the balnicity index is

$$\sigma_{\text{BI}}^2 = \int_{3000}^{25000} \left(\frac{\sigma_{f(v)}}{0.9} \right)^2 C \, dv \quad (5)$$

but uncertainties in the continuum usually dominate over this term.

Weymann et al. (1991) selected their minimum width and depth to avoid host and intervening systems at their spectral resolution, as well as noise in the data. With our

multiple-template fitting technique and somewhat higher resolution spectra, we may be able to reduce the minimum width and/or depth in our definition of intrinsic absorption. While we retain the Weymann et al. (1991) definition of traditional BALQSOs as quasars with $BI > 0$, we also present a modification of the BI which includes all absorption.

4.2. Testing Definitions of Broad Intrinsic Absorption

The ideal definition of broad intrinsic absorption was discussed in the appendix to Hall et al. (2002). It would include shallow troughs, “mini-BALs” which are not as wide as BALs yet may share all the rest of their properties, and absorption within 3000 km s^{-1} and beyond 25000 km s^{-1} of the systematic velocity as long as it was not confused with troughs from other transitions. This ideal definition of broad intrinsic absorption requires perfect knowledge of the systematic velocity, the continuum, and which troughs are truly intrinsic and which arise from host or intervening systems. The automated SDSS redshift determination scheme should produce consistent systemic velocities, and our system of continuum fitting with multiple templates is designed to address the problem of accurately estimating the continuum. However, we find two major difficulties in continuum fitting which require special attention: emission line regions and interpolated regions.

Both the CIV doublet (separation 497 km s^{-1}) and the MgII doublet (separation 768 km s^{-1}) almost always appear as a single broad emission line in quasar spectra. A minimum trough width of 450 km s^{-1} would ideally exclude all CIV features wherein the doublet was still distinct. Velocity spreads over $\sim 450 \text{ km s}^{-1}$ are very rare for intervening CIV systems and coincidences of multiple systems on these scales are uncommon because intervening narrow CIV absorbers are uncorrelated on velocity separations $> 400 \text{ km s}^{-1}$ (Churchill et al. 2000, Ding et al. 2003), so this minimum width would also exclude most intervening systems. Following the same reasoning, we arrive at a minimum intrinsic absorption width of 750 km s^{-1} for MgII.

However, the noise and variable resolution of our spectra, as well as poor continuum fits, might introduce false identifications if we adopt too narrow a minimum width. For example, if the CIV doublet was blended, we would not expect absorption narrower than 1000 km s^{-1} ; similarly, we would not expect absorption narrower than 1500 km s^{-1} for blended MgII doublets. We tested the lower three of these possible minimum widths: 450 km s^{-1} , 750 km s^{-1} , and 1000 km s^{-1} .

In addition to the minimum width of the trough, we must also define a minimum depth. If we define a shallow minimum depth, we risk identifying false troughs from noise and poor

continuum fits, but if we choose a minimum depth too deep, we risk missing weak troughs. Weymann et al. (1991) and Reichard et al. (2003a) used a minimum depth of 10% below the continuum. A 3σ minimum depth definition might be more reasonable for a sample which includes spectra with very different signal-to-noise ratios, but may result in different answers for repeat observations. We tested both 10% and 3σ minimum depths using the absorption index (AI) defined in §4.3.

Among the 16883 SDSS DR3 quasars in the CIV redshift range $1.7 \leq z \leq 4.38$, using the traditional 10% minimum depth, 60.6% have a nonzero absorption index (as defined in §4.3) for a minimum width of 450 km s^{-1} , 44.7% for a minimum width of 750 km s^{-1} , and 32.3% for a minimum width of 1000 km s^{-1} . With a 3σ minimum depth, the BALQSO fractions decrease significantly: 31.0% for a minimum width of 450 km s^{-1} , 26.4% for 750 km s^{-1} , and 20.2% for 1000 km s^{-1} . In comparison, only 12.0% of the 16883 quasars are identified as traditional BALQSOs. The number of quasars with nonzero BI for each binned value of AI are shown in Figure 3 for the different minimum widths and depths. Very few of the BALQSOs identified with a minimum depth of 450 km s^{-1} also have $\text{BI} > 0$. Because so many fewer quasars are identified for an error-dependent minimum depth of 3σ , we choose to retain the 10% minimum depth of the traditional balnicity.

A large number of distinct troughs could be attributed to intervening absorption systems and noise, and thus counting the number of troughs for each minimum width might provide a measure of the appropriateness of each minimum width. Figure 4 shows the number of troughs identified for each minimum width for both minimum depths. In both figures we see that a large number of troughs are identified using minimum widths of 450 km s^{-1} and 750 km s^{-1} . We conclude that the minimum widths of 450 km s^{-1} and 750 km s^{-1} are too aggressive for our quasar sample, and choose a minimum width of 1000 km s^{-1} for our definition of BALQSOs.

4.3. The Absorption Index

The “absorption index” (AI) was first proposed by Hall et al. (2002). In this paper, we modify that definition slightly so that AI is a true equivalent width, measuring all absorption within the limits of every trough, and so that the integration limit extends to 29000 km s^{-1} . Thus our AI is defined as:

$$\text{AI} = \int_0^{29000} [1 - f(v)] C' dv \quad (6)$$

where $f(v)$ is the normalized template-subtracted flux. The variable $C'(v)$ has the value $C' = 0$ except in contiguous troughs which exceed the minimum depth (10%) and the

minimum width (1000 km s^{-1}), in which case $C' = 1$. Zero velocity is defined using the SDSS redshift and the longest wavelength line of the doublet: 1550.77 \AA for C IV and 2803.53 \AA for Mg II.¹¹ The minimum AI is 100 km s^{-1} , and the maximum is 29000 km s^{-1} . The formal error of the absorption index is given by:

$$\sigma_{\text{AI}}^2 = \int_0^{29000} \sigma_{f(v)}^2 C' dv \quad (7)$$

Again, the error introduced by the continuum placement will dominate over this error term in most cases.

Even the most appropriate minimum depth and width may not successfully remove all contamination by noise-induced false troughs. For this reason we also calculated the reduced chi-squared of each trough:

$$\chi_{\text{trough}}^2 = \sum \frac{1}{N} \left(\frac{1 - f(v)}{\sigma} \right)^2 \quad (8)$$

Here N is the number of pixels in the trough and $f(v)$ is the normalized template-subtracted flux ($f(v) = 1$ where the sample flux and the template are equal, and $f = 0$ for a black trough). The greater the value of χ_{trough}^2 , the more likely the trough is not due to noise. We require that troughs have $\chi_{\text{trough}}^2 > 10$ to be considered true BALQSO troughs. After visual inspection, we find that 34 quasars with very low signal-to-noise ratio spectra have troughs which are wrongly eliminated by the $\chi_{\text{trough}}^2 > 10$ cut. We make an exception and do not require $\chi_{\text{trough}}^2 > 10$ for these 34 objects.

During the initial stages of BALQSO identification, we encountered a large number of false identifications within 5000 km s^{-1} of the emission line peak. This is caused by the difficulty of accurately fitting, in every quasar, the exact profile of the C IV or Mg II emission line. To avoid these false identifications we employ an extra minimum depth requirement in the emission line region. First we define a linear continuum across the emission region of the template which is an interpolated line across $\pm 5000 \text{ km s}^{-1}$ of the emission center. We then require absorption in this region to drop below the linear continuum by at least twice the noise level at least once within a trough, in addition to fulfilling the 1000 km s^{-1} minimum width and 10% minimum depth requirements. This method successfully repressed most of the false identifications in the line region.

¹¹Because the SDSS redshift is based on emission lines which can be blueshifted from the true systemic velocity, absorption can sometimes appear redward of zero velocity as defined above. We do not catalog such absorption unless it extends 1000 km s^{-1} shortward of the zero velocity wavelength.

Interpolated pixels are weighted out of the continuum-fitting process, but can still result in the misidentification of BAL troughs. Interpolation most often occurs in noisy areas of the spectrum, so it is possible that if the noise causes the two endpoints of an interpolated region wider than 1000 km s^{-1} to lie below the minimum depth, a BAL trough will be identified. To avoid these false identifications, we ignore all interpolated pixels during BAL trough identification. Recall from §2 that we extend the SDSS pipeline-interpolated regions by three pixels on either side.

We use the AI to identify both HiBALs with CIV absorption and LoBALs with absorption shortward of the MgII through our automated techniques. Figure 5 shows the general differences between quantifying our objects with the AI and BI. In most objects, $\text{AI} > \text{BI}$ because the AI includes all absorption in its definition and often identifies troughs which are too narrow to be identified using the BI. However, if a trough identified by the BI calculation has $\chi_0^2 < 10$ or is not deep enough within 5000 km s^{-1} of the line region, it is not considered a trough in the AI calculation. The automated fitting identified 138 objects with $\text{BI} > \text{AI}$ in the CIV region, and 137 $\text{BI} > \text{AI}$ objects in the MgII region. Visual inspection confirmed that these objects have only spurious troughs; therefore, they are not part of our BAL catalog. For the differences between the AI and BI for individual objects, see Figures 7 and 9, as well as the accompanying discussion in §5.1 and 5.2.

4.4. BALQSO Selection Summary

A summary of our selection of BALQSOs is presented in the list below.

1. From the DR3 QSO catalog, select all objects of $0.5 \leq z \leq 2.15$ for studies of absorption in the MgII region, and quasars of $1.7 \leq z \leq 4.38$ for the CIV region.
2. Weight emission lines and interpolated pixels according to Table 2.
3. Fit the DR1 quasar composite to the quasar, using the spectral index, reddening, and scale as free parameters. Weight out regions of absorption, identified as $\text{flux} \geq 4\sigma$ below the template in the region $\pm 5000 \text{ km s}^{-1}$ about the line center, and $\geq 2\sigma$ below the template in the region 5000 km s^{-1} to 29000 km s^{-1} .
4. Find the best-fit template from a set of 8 templates in the redshift bin. The templates are described in Table 1 and shown in Figures 1 and 2. The spectral index, reddening, and scale are free parameters in the fitting.
5. Independently scale the CIV or MgII emission line regions.

6. In the spectral region 0 km s^{-1} to 29000 km s^{-1} from the emission line center, identify regions of flux at least 10% below the continuum and 1000 km s^{-1} wide. Ignore interpolated pixels.
7. Eliminate from consideration any troughs less than 5000 km s^{-1} from the emission line center that do not have at least one pixel $> 2\sigma$ below a linear continuum across the emission region.
8. Eliminate from consideration any troughs with $\chi_0^2 < 10$ between the template and the quasar. (We relax this criterion for 25 objects with low signal-to-noise ratio spectra.)
9. Calculate the AI and BI.
10. Inspect all objects. Manually adjust the best-fit templates for quasars with poor automatic fits and repeat steps 6-9.

4.5. Other metrics

In addition to the measures of equivalent width provided by the absorption index and the traditional balnicity, other BALQSO quantities can be measured (e.g., Lee & Turnshek 1995). We calculated a number of additional metrics to learn which have the most relevance in the characterization of spectral absorption troughs:

- number of troughs
- v_{\min} and v_{\max} for each trough
- average fractional depth for each trough, given by $\Gamma_{\text{avg}} = \frac{\text{AI}_{\text{trough}}}{(v_{\max} - v_{\min})}$
- maximum fractional depth and maximum width of each trough and over the entire absorption region
- reduced chi-squared of the trough, given by $\chi^2 = \sum \frac{1}{N} \left(\frac{1-f}{\sigma} \right)^2$, with N the number of pixels in the trough
- weighted average velocity for each trough and over the entire absorption region, given by $v_{\text{wtavg}} = \frac{\int_0^{29000} v[1-f(v)]C' dv}{\text{AI}}$
- second moment for each trough, given by $\sigma_{\text{rms}}^2 = \frac{\int_0^{29000} (v - v_{\text{wtavg}})^2 [1-f(v)]C' dv}{\text{AI}}$

These metrics were measured on all objects of $AI > 0$. Discussion of metrics relevant to individual troughs are not presented here but will be discussed in a future paper (Hall et al. 2006).

5. BALQSO Catalog

Our entire BALQSO catalog is available electronically. Each column of the electronic table is described in Table 3. We present the first page of the catalog in tabular format in Table 4. We also include a supplementary Table of purely visually identified $z > 4.38$ BALQSOs in the Appendix.

The BAL subtype is coded in the catalog as follows: Lo denotes a LoBAL with $AI > 0$ in the MgII region; LoF denotes a FeLoBAL with $AI > 0$ in the MgII region; HLF denotes a FeLoBAL with $AI > 0$ in the CIV region; HL denotes a HiBAL in which broad ($\geq 1000 \text{ km s}^{-1}$) low-ionization absorption of Mg II, Al III or C II is also seen by visual inspection; Hi denotes a HiBAL-only object, in which broad low-ionization absorption is *not* seen even though Mg II is within the spectral coverage, and H denotes a HiBAL in which the Mg II region is not within the spectral coverage or has very low signal-to-noise ratio, and so whether or not the object is a LoBAL as well as a HiBAL is unknown. Thus, all CIV BAL measurements are coded with ‘H’, all MgII BAL measurements are coded with ‘Lo’, and the 86 $1.7 \leq z \leq 2.15$ quasars with both CIV and MgII BAL trough measurements have two entries in the catalog. There are a handful of $1.7 \leq z \leq 2.15$ LoBALs in Table 4 without an additional table entry for their CIV trough; these are all heavily reddened LoBALs with spectral signal-to-noise ratios too low in the CIV region to detect or measure a trough there. There are no known MgII-only BALQSOs in this or other BALQSO catalogs.

A significant number of BALQSOs in our catalog have troughs which are partially resolved individual absorption doublets. Such systems are sufficiently different from traditional BALs that some catalog users may prefer to exclude them, and we have therefore coded them with BAL subtype ‘n’. However, inspection shows that only a minority may be true catalog contaminants such as blends of two or more narrow absorption systems at very similar redshifts or intrinsically narrow systems included in the catalog due to imperfect fits of the nearby continuum. There are 51 such relatively narrow systems in the MgII catalog (11.2%) and 1069 such systems in the CIV catalog (24.6%). Further discussion on NALs in BALQSOs is presented by Ganguly et al. (2001).

We estimate that our catalog is $95 \pm 2\%$ complete based on two independent checks. First, among catalog LoBALs at $1.7 \leq z \leq 2.15$, $10 \pm 3\%$ were not originally also flagged

as HiBALs, and had to be added manually. However, proper fitting of the continuum of a HiBAL (necessary for trough identification) is most difficult for $z \lesssim 2$ quasars, when the C IV absorption region is close to the short-wavelength limit of the SDSS spectra, so a 10% loss rate is probably an overestimate for the entire catalog. Second, only 12 of 187 HiBALs ($6.5 \pm 2.1\%$) from Reichard et al. (2003a) which lie within our redshift range were not identified by our automated algorithm. Seven of those ($3.8 \pm 1.7\%$) were definite BALQSOs that we manually added to our catalog, and three of those seven had $z < 2$, where continuum fitting is most difficult. We adopt the weighted average of these completeness estimates: $95 \pm 2\%$.

We now discuss some individual examples of HiBALs, traditional HiBALs, LoBALs, and FeLoBALs. The frequencies of BAL phenomena given in the following subsections are raw only; a future paper will address the true frequencies, after correction for selection effects.

5.1. HiBALs

Among the 16883 quasars of the SDSS DR3 in the redshift range $1.7 \leq z \leq 4.38$, 1756 ($10.4 \pm 0.2\%$) are identified as traditional HiBALs, with a nonzero BI in the CIV region. This is a 3.5σ smaller fraction of traditional HiBALs than the $14 \pm 1\%$ identified by Reichard et al. (2003b) at $1.7 \leq z \leq 4.2$ in the SDSS EDR.

We identify 4386 HiBALs with $AI > 0$ in the CIV absorption region. This amounts to $26.0 \pm 0.3\%$ of quasars. The distribution of AI values among HiBALs is given by Figure 6. The observed distribution peaks at $AI \approx 400 \text{ km s}^{-1}$, past the minimum value of $AI = 100 \text{ km s}^{-1}$. However, it does not denote a peak in the true equivalent width distribution of BAL troughs because our sample does not include all objects at these AI values: absorption systems up to 999 km s^{-1} wide (less than the minimum width for the AI) can have AI values up to 999 km s^{-1} and yet are excluded from the plot. The AI distribution slowly tails off at large values, with no new trends for the region not shown ($AI \geq 4000 \text{ km s}^{-1}$).

Two non-BAL quasars, seven HiBALs, and one quasar with $BI > 0$ and $AI = 0$ from our catalog are displayed in Figure 7. All spectra are smoothed by 3 pixels. We discuss each object individually.

1. SDSS J014552.59–083536.8: This object is not a BALQSO, but shows the typical continuum fit for a normal CIV region.
2. SDSS J102038.73+094259.6: This quasar is not a BALQSO. The troughs in its spectrum are too narrow to be identified as intrinsic broad absorption by our algorithms.

3. SDSS J003832.26+152515.5: The broad troughs in this BALQSO make it a traditional BALQSO, but the AI is a better description than the BI because the AI includes the absorption within the minimum width and depth. Our line scaling method accurately fits the very weak CIV line.
4. SDSS J023252.80–001351.1: The spectrum of this object exhibits two wide and deep troughs near the emission line and a shallow and narrower trough around 15000 km s^{-1} from the emission peak. The BI computation includes only the two largest troughs, both of which are narrow enough that the inclusion of the minimum width and depth causes the AI to be much greater than the BI. This quasar is also a LoBAL.
5. SDSS J005010.54+153909.5: Although all the broad trough in this spectrum is identified in the traditional BALQSO definition, the AI is much greater than the BI because the BI calculation does not include the minimum width and depth.
6. SDSS J033917.02–051443.3: This quasar’s spectrum has low signal-to-noise, and we do not require the usual $\chi^2_{\text{trough}} > 10$ criterion in order to include the troughs in the AI calculation. The noise prevents any of the troughs from being wide enough to be included in the BI calculation.
7. SDSS J015024.43+004433.0: The wide, deep trough in its spectrum causes this object to be a traditional BALQSO as well as a BALQSO with $\text{AI} > 0$. However, the BI does not include the minimum depth, the minimum width, or the regions within 3000 km s^{-1} of the emission center, and therefore is a poorer characterization of the absorption than the AI. This quasar is also a LoBAL.
8. SDSS J131504.50+500239.5: The broad and deep trough in this quasar’s spectrum is within 3000 km s^{-1} , and the trough at 18000 km s^{-1} is narrower than 2000 km s^{-1} , so it is not identified as a traditional BALQSO. Both of these troughs are included in the AI calculation.
9. SDSS J075757.92+245128.8: This quasar spectrum has only a relatively narrow trough. While the trough is unlikely to be a contaminant, we designate this BALQSO as an ‘n’ subtype object. The trough is too narrow for this quasar to be a traditional BALQSO.
10. SDSS J203724.06–002053.2: A poor fit to the CIV emission line of this non-BALQSO causes the spurious identification of a trough from about $3000 - 5500 \text{ km s}^{-1}$ of the emission center. Our definition of the AI requires troughs within 5000 km s^{-1} to fall at least 2σ below a linear continuum interpolated over the region $\pm 5000 \text{ km s}^{-1}$ of the emission center, and therefore does not include this spurious trough. We identify 138

such objects with $BI > 0$ and $AI = 0$, all of which are not included in our BALQSO catalog because they contain only spurious troughs.

5.2. LoBALs

Only 191 non-spurious traditional LoBALs were identified via MgII. This represents just $0.55 \pm 0.04\%$ of the 34973 SDSS DR3 quasars in the redshift range $0.5 \leq z \leq 2.15$. The small fraction of LoBALs found using the traditional BI is not surprising, since MgII broad absorption troughs are known to be weaker and narrower than those found for CIV (Voit, Weymann, & Korista 1993). In addition, MgII absorption troughs typically occur nearer the systematic velocity, within 3000 km s^{-1} (Reichard et al. 2003a). For these reasons it is more appropriate to discuss our sample of LoBALs identified through the AI in the MgII region.

We identify 457 MgII LoBALs, or $1.31 \pm 0.06\%$ of quasars in our sample redshift range. Figure 8 gives the distribution of AI values for these LoBALs. The distribution peaks at nearly the same AI value as Figure 6 for BALQSOs, but tails off more swiftly, indicating that MgII troughs are not typically as wide and/or deep as CIV troughs. This is in agreement with other studies of LoBALs (e.g., Voit, Weymann, & Korista 1993).

Two non-LoBALs, seven LoBALs, and one traditional LoBAL with $AI = 0$ are shown in Figure 9 and discussed individually below.

1. SDSS J140935.07–010446.6: This quasar is a non-LoBAL (and a non-BALQSO as well), and it is representative of normal quasar spectrum and continuum fit in the region 2570–2830 Å.
2. SDSS J023252.80–001351.1: This object has no absorption in the MgII region and is therefore a non-LoBAL. However, in the CIV region (shown in Figure 7), this quasar has $AI = 4328 \text{ km s}^{-1}$ and is therefore a BALQSO. This quasar demonstrates that not all BALQSOs are LoBALs.
3. SDSS J013816.16+140431.6: This quasar spectrum exhibits a typical MgII absorption trough. When compared to typical CIV absorption troughs, most LoBALs (and this object in particular) exhibit absorption which is shallower, narrower, and nearer the emission region. The trough is too near the emission to be identified in the BI calculation.
4. SDSS J084842.13+010044.3: The troughs in this quasar spectrum are too narrow (even joined as they are) to be identified in the BI calculation, but they are included in the AI calculation.

5. SDSS J103824.47–010538.9: The spectrum of this quasar features several deep, narrow troughs. Although the troughs are unlikely to be caused by intervening systems, we designate this objects as a 'n' subtype LOBAL. None of these troughs is sufficiently wide enough for a BI-based identification.
6. SDSS J120928.11+003511.5: Despite the low signal-to-noise ratio of this quasar spectrum, a broad absorption trough is identified near the emission region. This trough is too shallow for identification by the BI.
7. SDSS J130741.12+503106.5: This quasar is one of the few LoBALs with $BI > 0$ as well as $AI > 0$. However, of its obvious broad absorption trough, only the small part bluer than 3000 km s^{-1} of the emission line is included by the BI calculation. The AI provides a much better metric of the absorption than the BI.
8. SDSS J143751.16+530706.8: This quasar spectrum exhibits two broad, deep troughs. Although the quasar is identified as a traditional BALQSO, the AI includes the minimum depth and width of each trough in its calculation, and better characterizes the absorption than the BI. This quasar is also a FeLoBAL.
9. SDSS J220931.92+125814.5: The absorption trough in the quasar spectrum is broad, but rather shallow compared to the other LoBALs shown here. Since the AI includes the minimum depth and width in its calculation, it provides a much better description of the absorption in this quasar than the BI.
10. SDSS J081525.94+363515.1: This non-BALQSO has $BI > 0$ but $AI = 0$. The nonzero BI identifies a spurious trough from about $3000 - 6000 \text{ km s}^{-1}$ of the emission center. This region is below the fitted continuum only because of the inadequate fit to an asymmetric emission profile. The AI definition, however, requires that absorption troughs within 5000 km s^{-1} of the emission center fall at least 2σ below a linear continuum interpolated over the region $\pm 5000 \text{ km s}^{-1}$. We identify 137 $BI > AI$ objects in the MgII region, all of which have only spurious troughs and are not included in our BALQSO catalog.

5.3. FeLoBALs

We searched for FeLoBALs by visual inspection of our BALQSO sample. We identified 138 unique confirmed and candidate FeLoBALs, one of which (SDSS J094317.60+541705.1) was added to the catalog by hand since its spectrum shortward of MgII is completely oblit-

erated by overlapping troughs. Up to $0.33 \pm 0.03\%$ of SDSS quasars at $0.5 \leq z \leq 4.38$ are FeLoBALs. Five FeLoBALs are shown in Figure 10 and are discussed below.

1. SDSS J031856.62–060037.7: The spectrum of this FeLoBAL exhibits several deep troughs associated with C IV, Al III, Mg II, C III], Fe II, and Fe III. Although the AI in the Mg II region is likely accurate, the widespread absorption causes the continuum to be slightly underestimated outside the Mg II region, since absorption is only weighted out of the fitting in the Mg II region. This quasar is discussed in more detail by Hall et al. (2002).
2. SDSS J115436.60+030006.3: The absorption troughs in the spectrum of this FeLoBAL are extremely broad and overlap, with only a small fraction of the spectrum remaining unabsorbed. The Mg II emission is almost invisible due to absorption from Mg I $\lambda 2853$ Å absorption. The continuum is greatly underestimated in the fitting. Further discussion for this quasar can be found in Hall et al. (2002).
3. SDSS J135246.37+423923.5: The absorption troughs in the spectrum of this quasar are very broad, although they are not quite so deep or overlapping as those of SDSS J1154+0300. Many of the troughs also appear more blueshifted, so that the C IV, C III], and Mg II emission is more apparent than in the other FeLoBALs shown here.
4. SDSS J150848.80+605551.9: With several deep and relatively narrow troughs, this quasar appears to be a more heavily reddened version of the FeLoBAL SDSS J0318–0600. As in SDSS J0318–0600, the continuum is only slightly underestimated in the fit to this FeLoBAL.
5. SDSS J171701.00+304357.6: The spectrum of this FeLoBAL exhibits broad, deep troughs throughout the spectrum. The continuum fit is very poor, and the absorption in both the C IV and the Mg II regions are probably underestimated.

5.4. Manually Included Objects

We visually inspect the best template fits for all quasars, and adjust the best-fit templates for 347 quasars in the C IV region and 3 quasars in the Mg II region. In some cases the quasar has an unusual emission line profile and the automatically scaled emission line of the best-fit template is manually adjusted to prevent over- or under-estimation of the AI. In other objects, the normalization region of the quasar spectrum (used to determine the scale factor) is especially noisy, and the continuum scale must be adjusted. In Figure 11 we display

five quasars in the CIV region with their automatic best-fit templates and their manually adjusted best-fit templates. Each object shown in Figure 11 is individually discussed below.

1. 031842.79–074030.7: The CIV emission region is contaminated by narrow $H\beta$ emission from an emission-line galaxy along the line of sight, which causes the automatically determined best-fit template to over-estimate the AI. We manually reduce the line scaling of the best-fit template to accurately determine the AI of this BALQSO.
2. 085008.33+023522.9: The automatically scaled emission line region does not accurately represent the CIV line profile of this quasar. We adjust the line scaling and more accurately determine the AI.
3. 093552.97+495314.3: Widespread broad absorption causes the best-fit template continuum to be underestimated between the SiIV and CIV emission lines. We increase the scaling factor in order to measure all of the absorption.
4. 094456.75+544118.0: While the absorption is not so widespread as in the previous object, the best-fit template continuum is still underestimated and this object is falsely determined to be a non-BALQSO. After manually adjusting the scaling factor, this quasar is correctly classified as a BAL with a shallow trough.
5. 100619.30+625335.0: This is one of the few objects for which the automatic template fitting failed for no obvious reason. The manually adjusted template provides an accurate continuum from which to measure the AI.

6. Discussion: Spectral Properties of BALQSOs

The size of our catalog presents the opportunity for a statistical study of the nature of BALQSOs. In this paper we study what can be learned directly from the results of the fitting process; in Hall et al. (2006, in preparation) we address issues that require additional analysis.

We investigate the spectral properties of the BALQSOs in our sample by comparing their properties to those of the non-BALQSOs in our parent data set. Figure 12 shows the distribution of BALQSOs with the best-fitting template, spectral index, and reddening (the latter two parameters are highly degenerate and not necessarily physical). Figure 13 shows the same distributions of LoBALs. We include only BALQSOs and LoBALs of spectral $\text{SNR} > 9$ because the low signal-to-noise BALQSOs and LoBALs that we identify may be preferentially more luminous, with correspondingly broader emission lines. Figures 12 and

13 should therefore have no artificial luminosity effects caused by our fitting constraints. The top histograms indicate that BALQSOs and LoBALs favor a continuum fit by the more luminous and widest line width template. We interpret this as a fit to wider line width templates in general: since line width is correlated with luminosity, less luminous BALQSOs and LoBALs with wider line widths may prefer a fit by more luminous templates instead of the less luminous widest line width template. This preference suggests that BALQSOs and LoBALs have broader emission lines than other quasars. If the emission-line width depends in part on the orientation of a disk-like emission region to our line of sight (Murray & Chiang 1998; Peterson 2003), this preference suggests that broad absorption troughs are preferentially observed along low-latitude sightlines above the disk. This preference is also consistent with previous work: Richards et al. (2002) showed that quasars with large systematic emission line blueshifts tend to have broader lines, and Reichard et al. (2003b) showed that BALQSOs tend to have large systematic blueshifts.

Since the spectral index and reddening are degenerate in our fitting algorithms, we study the properties of both with regards to BALQSOs, LoBALs, and non-BALQSOs through Figure 14. While most LoBALs and BALQSOs are located within the contours of the non-BALQSO population, a large fraction of BALQSOs are shifted to the upper left of the plot, indicating that BALQSOs on average are more intrinsically reddened than non-BALQSOs similar to the result of Reichard et al. (2003b). A two-dimensional Kolmogorov-Smirnov (K-S) statistical test (Press et al. 1998) on the spectral index and reddening distribution reveals probabilities of less than 10^{-7} that BALQSOs and non-BALQSOs share the same spectral index and reddening distribution, or that LoBALs and non-BALQSOs share the same distribution, or that LoBALs and BALQSOs share the same distribution. The shift of BALQSOs in spectral index-reddening space creates a selection effect that must be corrected in order to produce a true fraction of BALQSOs.

7. Conclusions

1. Our definition of broad absorption allows for the identification and characterization of absorption troughs near the emission line peak and as narrow as 1000 km s^{-1} . The AI provides a more complete description of broad absorption than the traditional BI.
2. BALQSOs defined by $\text{AI} > 0$ comprise approximately 26% of quasars, MgII LoBALs about 1.3%, and FeLoBALs about 0.3%. These are raw fractions only, and do not take into account the larger average reddening seen in BALQSOs as compared to non-BALQSOs.
3. BALQSOs appear to have wider emission lines than non-BALQSOs, on average. This

supports an AGN model in which the broad emission and absorption regions are in a disk-like configuration.

We thank the referee for many helpful comments. This research was partially supported by grant NSF AST03-07582 (JRT, DPS, DVB). JRT acknowledges support from a Schreyer’s Honors College Summer Research Scholarship. PBH acknowledges support from a NSERC Discovery Grant. GTR was supported in part by a Gordon and Betty Moore Fellowship in Data Intensive Sciences.

Funding for the creation and distribution of the SDSS Archive has been provided by the Alfred P. Sloan Foundation, the Participating Institutions, the National Aeronautics and Space Administration, the National Science Foundation, the U.S. Department of Energy, the Japanese Monbukagakusho, and the Max Planck Society. The SDSS Web site is <http://www.sdss.org/>.

The SDSS is managed by the Astrophysical Research Consortium (ARC) for the Participating Institutions. The Participating Institutions are The University of Chicago, Fermilab, the Institute for Advanced Study, the Japan Participation Group, The Johns Hopkins University, the Korean Scientist Group, Los Alamos National Laboratory, the Max-Planck-Institute for Astronomy (MPIA), the Max-Planck-Institute for Astrophysics (MPA), New Mexico State University, University of Pittsburgh, University of Portsmouth, Princeton University, the United States Naval Observatory, and the University of Washington.

A. Supplementary list of visually identified HiBALs at $z > 4.38$

The upper limit redshift of our BAL catalog is $z = 4.38$. BALQSOs can be identified at higher redshifts in SDSS spectra, but calculating their AI or BI values is difficult since normalization and continuum fitting of high-redshift spectra can be problematic. Nonetheless, to further the study of BALQSOs at all redshifts we provide in Table 5 a list of 32 BALQSOs and 7 BALQSO candidates visually identified from the 213 $z > 4.38$ quasars in the SDSS DR3 quasar catalog. Only one, or possibly two, can be identified as LoBALs from the SDSS spectra alone.

The raw fraction of HiBALs at $z > 4.38$ is $15.0^{+2.9}_{-2.5}\%$, higher than but consistent with the fraction at lower redshifts. However, SDSS spectra of $z > 4.38$ quasars are generally of lower signal-to-noise ratio than SDSS spectra of lower-redshift HiBALs (average i -band signal-to-noise ratios 5.7 ± 2.8 vs. 9.9 ± 5.6 , respectively). Therefore, weak BAL troughs will be *underrepresented* in our $z > 4.38$ sample and the true incidence of HiBALs in it will

be even larger, perhaps indicating a real increase in the HiBAL fraction at high redshift. Careful study of even larger samples of BALQSOs will be needed to put this possibility on firm statistical footing.

REFERENCES

- Abazajian, K., et al. 2003, *AJ*, 126, 2081
- Abazajian, K., et al. 2005, *AJ*, 129, 1755
- Baldwin, J. A. 1977, *ApJ*, 214, 679
- Becker, R. H., White, R. L., Gregg, M. D., Brotherton, M. S. et al. 2000, *ApJ*, 538, 72
- Blanton, M. R., Lupton, R. H., Maley, F. M., Young, N., Zehavi, I., and Loveday, J. 2003, *AJ*, 125, 2276
- Boroson, T. A. & Meyers, K. A. 1992, *ApJ*, 397, 442
- Brandt, W. N., Laor, A., Wills, B. J. 2000, *ApJ* 528, 637
- Cardelli, J. A., Clayton, G. C., and Mathis J. S. 1989, *ApJ* 345, 245
- Churchill, C. W., Mellon, R. R., Charlton, J. C., Jannuzi, B. T., Kirhakos, S., Steidel, C. C., & Schneider, D. P. 2000, *ApJ*, 543, 577
- Croom, S. M., Smith, R. J., Boyle, B. J., Shanks, T., Miller, L., Outram, P. J., & Loaring, N. S. 2004, *MNRAS*, 349, 1397
- Ding, J., Charlton, J. C., Churchill, C. W., & Palma, C. 2003, *ApJ*, 590, 746
- Fukugita, M., Ichikawa, T., Gunn, J. E., Doi, M., Shimasaku, K., & Schneider, D. P. 1996, *AJ*, 111, 1748
- Gallagher, S. C., Brandt, W. N., Chartas, G., & Garmire, G. P. 2002, *ApJ*, 567, 37
- Ganguly, R., Bond, N. A., Charlton, J. C., Eracleous, M., Brandt, W. N., & Churchill, C. W. 2001, *ApJ*, 549, 133
- Gunn, J. E., et al. 1998, *AJ*, 116, 3040
- Gunn, J. E., et al. 2006, *AJ*, 131, in press
- Hall, P. B., Anderson, S. F., Strauss, M. A., York, D. G. et al. 2002, *ApJS*, 141, 267

- Hall, P. B., Trump, J. R., Richards, G. T., Proga, D., Reichard, T. A., Vanden Berk, D. E., & Schneider, D. P. 2006, in prep.
- Hazard, C., Morton, D. C., Terlevich, R., & McMahon, R. 1984, *ApJ*, 282, 33
- Hewett, P. C. & Foltz, C. B. 2003, *AJ*, 125, 1784
- Hogg, D. W., Schlegel, D. J., Finkbeiner, D. P., & Gunn, J. E. 2001, *AJ*, 122, 2129
- Hopkins et al. 2004, *AJ*, 128, 1112
- Ivezić, Z., et al. 2004, *AN*, 325, 583
- Lee, L. W. & Turnshek, D. A. 1995, *ApJL*, 453, L61
- Lupton, R. H., Gunn, J. E., & Szalay, A. S. 1999, 1999, *AJ*, 118, 1406
- Lupton, R. H., Gunn, J. E., Ivezić, Ž., Knapp, G. R., Kent, S., & Yasuda, N. 2001, in ASP Conf. Ser. 238, *Astronomical Data Analysis Software and Systems*, eds. F. R. Harnden, F. A. Primini, & H. E. Payne (San Francisco:ASP), 269
- Marziani, P., Sulentic, J. W., Zamanov, R., Calvani, M., Dultzin-Hacyan, D., Bachev, R., & Zwitter, T. 2003, *ApJS*, 145, 199
- Menou, K., et al. 2001, *ApJ*, 561, 645
- Murray, N. & Chiang, J. 1998, *ApJ*, 494, 125
- Osmer, P. S., Porter, A. C., & Green, R. F. 1994, *ApJ*, 436, 678
- Pei, Y. C. 1992, *ApJ*, 395, 130
- Peterson, B. M. 2003, in ASP Conf. Ser. 290, *Active Galactic Nuclei: From Central Engine to Host Galaxy*, eds. S. Collin, F. Combes & I. Shlosman (San Francisco:ASP), 43
- Pier, J. R., Munn, J. A., Hindsley, R. B., Hennessy, G. S., Kent, S. M., Lupton, R. H., & Ivezić, Ž., 2003, *AJ*, 125, 1559
- Press, W. H., Teukolsky, S. A., Vetterling, W. T., & Flannery, B. P. 1992, *Numerical recipes in C. The art of scientific computing* (Cambridge: University Press, 1992, 2nd ed.)
- Prevot, M. L., Lequeux, J., Prevot, L., Maurice, E., & Rocca-Volmerange, B. 1984, *A&A*, 132, 389
- Reichard, T. A., et al. 2003, *AJ*, 120, 1711

- Reichard, T. A., et al. 2003b, AJ, 126, 2594
- Richards, G. T., et al. 2001, AJ, 121, 2308
- Richards, G. T., et al. 2002, AJ, 123, 2945
- Richards, G. T., Hall, P. B., Reichard, T. A., & Vanden Berk, D. E. 2004, in ASP Conf. Ser. 311, AGN Physics with the SDSS Conf. Proc., eds. G. T. Richards & P. B. Hall, (San Francisco:ASP), 25
- Richstone, D. O. & Schmidt, M. 1980, ApJ, 235, 361
- Schlegel, D. J., Finkbeiner, D. P., & Davis, M. 1998, ApJ, 500, 525
- Schneider, D. P., et. al. 2002, AJ, 123, 567
- Schneider, D. P., et. al. 2003, AJ, 126, 2579
- Schneider, D. P., et. al. 2005, AJ, 130, 367
- Sigut, T. A. A., Pradhan, A. K., & Nahar, S. N. 2004, ApJ, 661, 81
- Smith, J. A., et al. 2002, AJ, 123, 2121
- Sprayberry, D. & Foltz, C. B. 1992, ApJ, 390, 39
- Spergel, D. N., et al. 2003, ApJ, 148, 175
- Stoughton, C. et al. 2002a, AJ, 123, 485
- Stoughton, C. et al. 2002b, SPIE, 4836, 339
- Tolea, A., Krolik, J. H., & Tsvetanov, Z. 2002, ApJL, 578, 31
- Tucker, D., et al. 2006, PASP, submitted
- Vanden Berk, D. E. et al. 2001, AJ 122, 549
- Vanden Berk, D. E., Yip, C. W., Connolly, A. J., Jester, S., & Stoughton, C. 1994, AGN Physics with the SDSS Conf. Proc., eds. G. T. Richards & P. B. Hall, 21
- Vestergaard, M. & Wilkes, B. J. 2001, ApJS, 134, 1
- Voit, G. M., Weymann, R. J., & Korista, K. T. 1993, ApJ, 413, 95
- Weymann, R. J., Morris, S. L., Foltz, C. B., & Hewitt, P. C. 1991, ApJ, 373, 23

York, D. G., et al. 2000, AJ, 120, 1579

Table 1. Quasar Template Properties

Composite $z_{\min} - z_{\max}$	Fitting $z_{\min} - z_{\max}$	Region to fit	Avg. # per template
2.30-4.90	2.30-4.38	C IV	56
1.90-2.30	1.90-2.30	C IV	410
1.52-1.90	1.70-1.90	C IV	372
1.40-2.20	1.40-2.15	Mg II	1576
0.90-1.40	0.90-1.40	Mg II	1552
0.39-0.90	0.50-0.90	Mg II	1279

Table 2. Wavelength Region Weights

λ_i (Å)	λ_f (Å)	Weight	Description
0	1055	0.0	Ly β and bluer
1055	1160	0.0	Ly α forest
1160	1240	0.0	Ly α emission, N V blue wing
1240	1290	0.5	N V red wing
1290	1360	1.0 ^a	Si IV absorption region
1360	1402	0.0	Si IV/O IV] blue wing
1402	1446	0.5	Si IV/O IV] red wing
1425	1524	1.0 ^b	C IV absorption region
1524	1577	1.0 ^b	C IV emission
1750	1830	0.5	Al III absorption region
1830	1857	0.0	C III] Fe III blue wing
1857	1976	0.5	C III] Fe III red wing
2579	2757	1.0 ^c	Mg II absorption region
2757	2850	1.0 ^c	Mg II emission
3394	3446	0.0	[Ne V] emission
3714	3740	0.0	[O II] emission
3850	3884	0.0	[Ne III] emission
4050	9200	0.0	H δ , beyond power-law
$\sigma(\lambda) = 0$		0.0	Interpolated pixels

^aVelocities in the Si IV region corresponding to regions of flux identified with absorption in the C IV region were assigned $w(\lambda) = 0$.

^bRegions of flux below the first-pass fit by 4σ or more were assigned $w(\lambda) = 0$.

^cRegions of flux 2σ or more below a linear continuum from ± 5000 km s⁻¹ of the emission line in the first-pass fit were assigned $w(\lambda) = 0$, and regions above this threshold were assigned $w(\lambda) = 0.5$.

Table 3. SDSS DR3 BALQSO Electronic Catalog Format

Column	Format	Description
1	A18	SDSS DR3 Designation hhmmss.ss+ddmmss.s (J2000)
2	I4	Spectroscopic Plate Number
3	I5	Modified Julian Date of spectroscopic observation
4	I3	Spectroscopic Fiber Number
5	F5.3	Redshift
6	F5.2	PSF i magnitude (not corrected for Galactic extinction)
7	F6.2	Absolute i magnitude
8	A4	Subtype ^a H for HiBAL sample, Lo for LoBAL sample, F for FeLoBAL
9	I6	Absorption Index, AI (km s^{-1})
10	F6.2	Error in the Absorption Index, σ_{AI} (km s^{-1})
11	I6	Balnicity Index, BI (km s^{-1})
12	F6.2	Error in the Balnicity Index, σ_{BI} (km s^{-1})
13	I1	Best-fit template number
14	F6.2	Spectral index α_ν used by the best-fit template
15	F6.3	Reddening $E(B - V)$ used by the best-fit template
16	F7.2	χ_0^2 value of the best fit
17	I2	Number of distinct BAL troughs
18	I5	Widest BAL trough (km s^{-1})
19	F4.2	Deepest part of any BAL trough
20	I6	Weighted average velocity of the BAL troughs (km s^{-1})
21	I6	Maximum velocity of the BAL troughs from the emission line (km s^{-1})
22	F4.1	SDSS spectrum signal-to-noise ratio in the i -band

^aFor full details on subtype codes, see §5 and Table 4.

Table 4. SDSS DR3 BALQSO catalog (page 1)

Quasar (SDSS J)	Spectrum ^a	z	i	M_i	Type ^b	AI	BI	T ^c	α_ν	$E(B-V)$	$\chi^2_{0,\text{fit}}$	n^d	widest	deepest	v_{wtavg}	v_{max}
000009.26+151754.5	751-52251-354	1.199	19.17	-25.08	Lo	1693	0	3	-0.97	-0.059	1.27	1	4141	0.82	2217	4797
000056.89-010409.7	387-51791-098	2.106	19.28	-26.29	Hi	4733	1076	0	0.61	0.160	1.93	1	7453	1.00	4439	8639
000103.85-104630.3	650-52143-133	2.081	18.15	-27.38	Hi	1222	0	4	-0.36	0.022	2.17	1	3451	0.66	2619	4287
000119.64+154828.8	750-52235-566	1.924	19.02	-26.34	HL	7299	5402	0	0.44	0.091	1.61	1	12067	0.91	9291	15417
000119.64+154828.8	750-52235-566	1.924	19.02	-26.34	Lo	502	0	0	0.41	0.120	2.43	2	1172	0.36	10321	11737
000303.35-105150.6	650-52143-048	3.647	19.25	-27.53	H	1808	0	0	-7.13	-0.450	3.42	2	2277	0.91	5588	14961
000335.20+144743.6	750-52235-036	3.484	20.07	-26.67	nH	758	0	7	2.95	0.246	1.25	1	1518	0.79	859	1603
000913.76-095754.5	651-52141-519	2.069	18.68	-26.85	Hi	3724	852	7	-0.70	-0.018	1.44	1	8005	0.71	4631	8982
001025.90+005447.6	389-51795-332	2.847	18.94	-27.26	H	4787	2557	1	-1.61	-0.076	4.15	2	5241	0.88	11439	17378
001053.56+000642.9	389-51795-348	1.879	18.98	-26.30	nHi	454	0	6	-0.49	0.006	1.46	1	1864	0.57	2245	3326
001130.55+005550.7	389-51795-339	2.309	18.34	-27.41	Hi	2351	32	7	-3.20	-0.174	2.67	1	4900	0.90	3321	6275
001134.52+155137.4	752-52251-378	4.325	20.09	-27.12	H	1173	0	7	-6.92	-0.433	3.09	1	3080	0.74	27425	28948
001306.15+000431.9	388-51793-624	2.165	18.48	-27.12	Hi	399	0	7	0.91	0.069	1.63	1	1378	0.61	13012	13732
001328.21+135827.9	752-52251-204	3.576	18.94	-27.83	H	301	0	7	1.16	0.097	1.39	1	1381	0.31	3029	3717
001400.45+004255.4	389-51795-412	1.710	18.34	-26.71	Hi	494	0	6	-0.24	-0.019	1.29	1	2261	0.40	26174	27307
001408.22-085242.2	652-52138-363	1.745	18.40	-26.72	Hi	3288	0	0	-0.23	0.203	0.00	1	4141	1.00	3866	5954
001438.28-010750.1	389-51795-211	1.816	18.48	-26.76	Hi	3045	8	4	0.46	0.174	2.19	2	3381	1.00	3810	6155
001502.26+001212.4	389-51795-465	2.852	18.84	-27.38	H	2198	717	6	-2.37	-0.144	2.32	1	4415	1.00	7607	10127
001528.86-090332.8	652-52138-403	2.000	19.26	-26.20	HL	6056	4834	7	1.54	0.282	1.41	1	8617	1.00	10374	15034
001528.86-090332.8	652-52138-403	2.000	19.26	-26.20	Lo	1181	189	1	2.15	0.394	1.55	2	3310	0.52	8994	11698

^aThe SDSS spectrum is designated by its plate-mjd-fiber.

^bThe BAL subtype. The code n denotes a relatively narrow trough, LoF denotes a FeLoBAL with Mg II absorption in its SDSS spectra; HLF denotes a FeLoBAL with C IV absorption in its SDSS spectra; Lo denotes a LoBAL detected through Mg II absorption; HL denotes a HiBAL in which broad ($\geq 1000 \text{ km s}^{-1}$) low-ionization absorption is also seen; Hi denotes a HiBAL-only object, in which broad low-ionization absorption is *not* seen even though Mg II is within the spectral coverage, and H denotes a HiBAL in which the Mg II region is not within the spectral coverage or has a very low signal-to-noise ratio and so whether or not the object is a LoBAL as well as a HiBAL is unknown.

^cThe best-fitting template number. Template numbers 0-3 correspond to the less luminous bin and numbers 4-7 to the more luminous bin; line width increases from 0 to 3 and from 4 to 7.

^dThe number of identified broad absorption troughs.

Table 5. Manually Identified $z > 4.38$ BALQSOs from the SDSS DR3 Quasar Catalog

Quasar (SDSS J)	Spectrum ^a	z	i	M_i	Type ^b
001714.67–100055.4	652-52138-152	5.0105	19.523	–27.935	H
012004.82+141108.2	424-51893-270	4.7293	20.199	–27.131	H
082234.47+361534.8	826-52295-540	4.5995	19.934	–27.385	H?
085634.92+525206.2	449-51900-246	4.8166	20.287	–27.045	H
092819.28+534024.2	554-52000-620	4.3900	19.530	–27.598	H
093333.86+051839.9	992-52644-156	4.4900	19.360	–27.869	H
095151.18+594556.1	453-51915-586	4.8593	19.817	–27.520	H?
101053.52+644832.0	488-51914-474	4.6848	19.848	–27.469	H
102343.13+553132.3	946-52407-027	4.4550	19.315	–27.835	HL
103601.03+500831.8	875-52354-474	4.4695	19.218	–27.943	H
110041.96+580001.0	949-52427-031	4.7706	19.970	–27.319	H?
110628.67+554054.8	908-52373-189	4.5481	20.056	–27.136	H
110826.31+003706.7	278-51900-435	4.3950	19.780	–27.385	H
111523.24+082918.4	1222-52763-241	4.6400	19.574	–27.730	H
112956.09–014212.4	327-52294-337	4.8838	19.685	–27.716	H
114448.54+055709.8	839-52373-413	4.7904	20.189	–27.133	H?
120131.56+053510.1	842-52376-323	4.8303	19.455	–27.875	H
120715.45+595342.9	954-52405-178	4.4833	20.157	–27.026	H
121422.02+665707.5	493-51957-103	4.6389	18.876	–28.370	H
123937.17+674020.8	494-51915-542	4.4235	20.170	–26.975	H
124400.05+553406.8	1038-52673-371	4.6250	19.609	–27.629	H
125850.93+615738.5	783-52325-316	4.4905	20.069	–27.113	HL?
132853.66–022441.6	911-52426-266	4.6945	19.841	–27.485	H
133304.50+604736.1	785-52339-149	4.4219	20.130	–27.012	H?
135249.81–031354.3	914-52721-205	4.7477	19.798	–27.555	H
141914.18–015012.6	917-52400-489	4.5860	19.092	–28.215	H
142535.97–023934.4	918-52404-260	4.7500	19.425	–27.975	H
142935.55+435628.9	1288-52731-248	4.6410	20.048	–27.194	H
143352.20+022713.9	536-52024-346	4.7215	18.331	–29.003	H?
144717.97+040112.4	587-52026-556	4.5800	19.168	–28.091	H
151035.29+514841.0	1165-52703-475	5.0314	20.029	–27.400	H

Table 5—Continued

Quasar (SDSS J)	Spectrum ^a	z	i	M_i	Type ^b
151404.78+473815.8	1330-52822-129	4.6673	19.702	−27.589	H
160120.09+374948.9	1055-52761-308	4.4187	19.953	−27.193	H
160501.20−011220.7	344-51693-054	4.9218	19.798	−27.956	H
165354.61+405402.1	631-52079-127	4.9768	18.648	−28.762	H
223521.22−082127.2	722-52224-388	4.4247	19.839	−27.382	H
224147.75+135202.7	739-52520-557	4.4480	18.786	−28.451	H ^c
224255.52+124225.6	739-52520-059	4.4332	19.305	−27.914	H
235152.80+160048.9	749-52226-417	4.6939	19.682	−27.635	H?

^aThe SDSS spectrum is designated by its plate-mjd-fiber.

^bThe Type column gives information on the subtype of the BALQSO. ‘H’ denotes a HiBAL, ‘H?’ denotes a candidate HiBAL, ‘HL’ denotes a confirmed LoBAL, and ‘HL?’ a possible LoBAL. Note that ‘H’ objects could still turn out to be LoBALs: a definitive classification requires spectral coverage of the Al III and Mg II regions, which is not available.

^cThe C IV absorption trough in this object is at $v > 29,000 \text{ km s}^{-1}$, and so this BALQSO would not have been included in our main catalog even if it had been at $z < 4.38$.

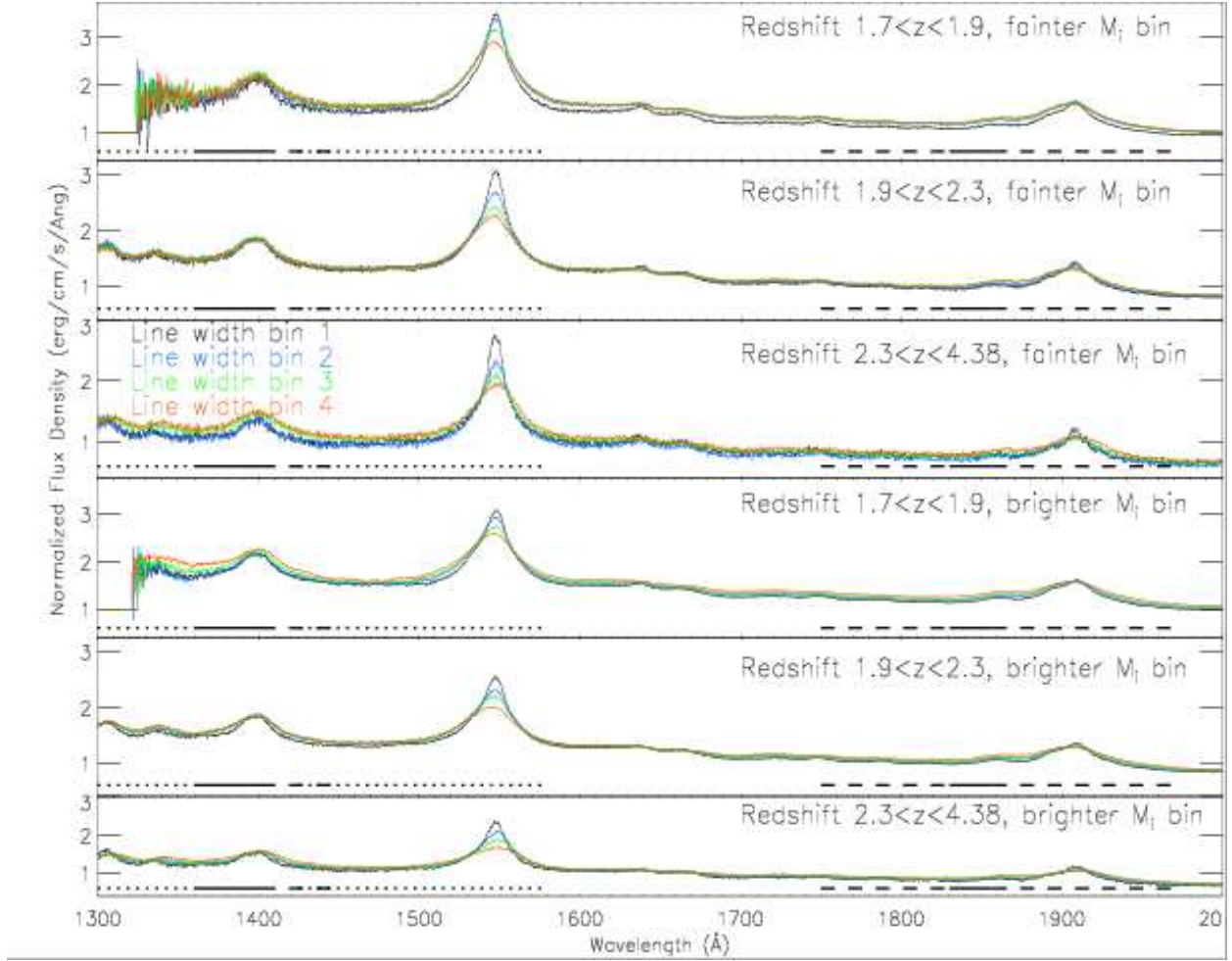


Fig. 1.— The templates used in fitting for CIV absorption, as described in Table 1. The four line width bins are shown by different colors in each plot, from narrowest to broadest. Each set of three redshift bins goes down the page with increasing redshift. The top three plots are in the less luminous absolute i-band bin. The templates are plotted for the CIV absorption region and include the $1710 \pm 10 \text{ \AA}$ normalization window. Below each spectrum are lines representing the weights: the solid lines represent $w(\lambda) = 0$ regions, the dashed lines are $w(\lambda) = 0.5$, and the dotted lines are the special CIV and SiIV absorption regions, according to Table 2 and §3.2. The spectral resolution is ≈ 2000 .

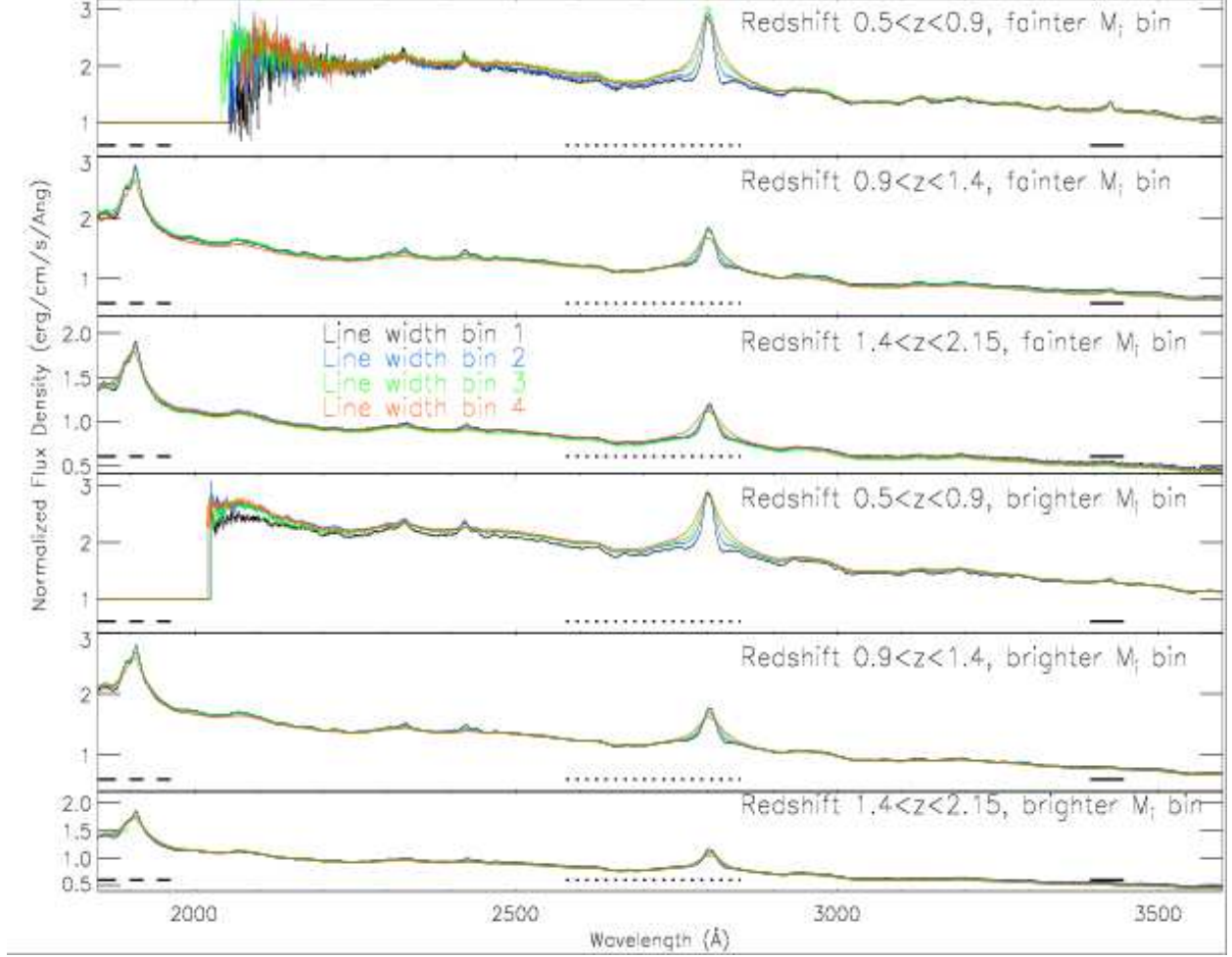


Fig. 2.— The templates for MgII absorption, as described in Table 1. As in Figure 1, each plot has four line-width bins and the top three plots, descending with increasing redshift, are in the less luminous absolute i-band bin. The templates extend over the MgII absorption region and include the $2910 \pm 10 \text{ Å}$ normalization window. Below each spectrum the solid lines represent $w(\lambda) = 0$ regions, the dashed lines are $w(\lambda) = 0.5$, and the dotted lines are the special MgII emission and absorption region, according to Table 2 and §3.2.

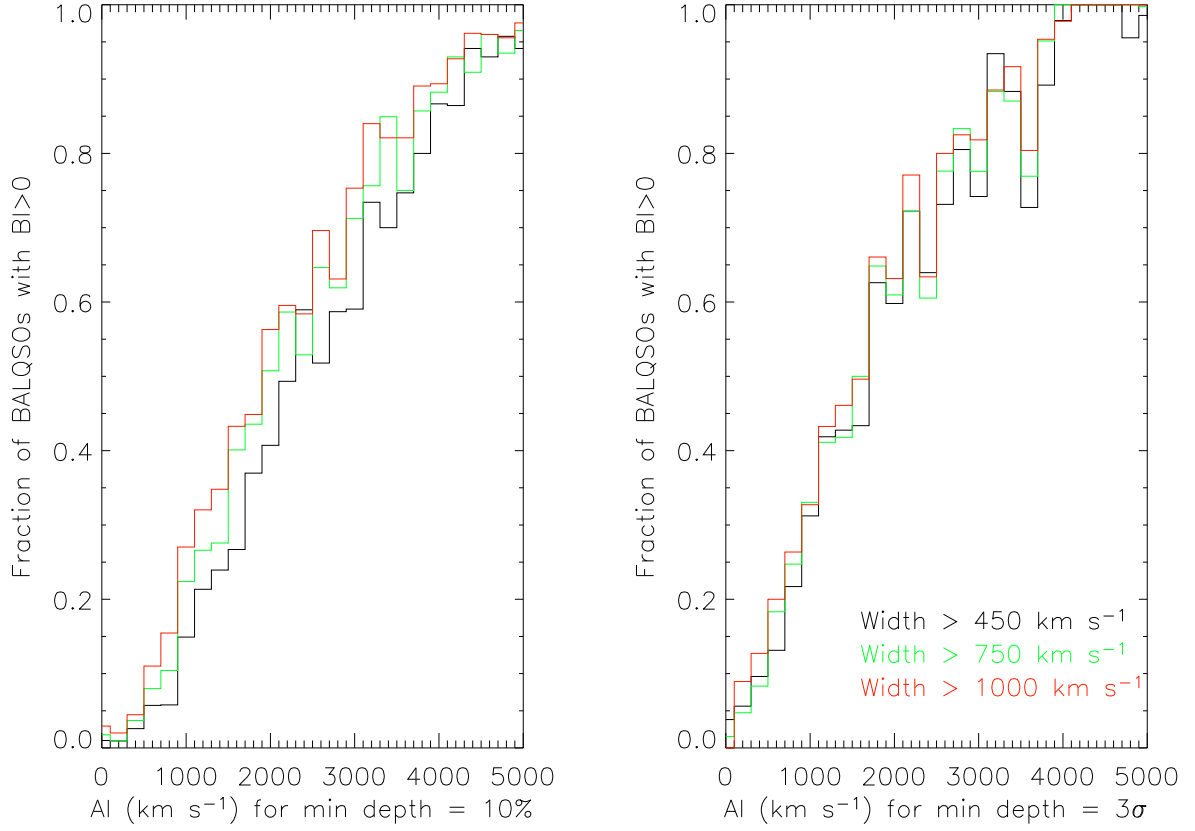


Fig. 3.— The AI distribution of BALQSOs which also have $BI > 0$ for varying minimum widths. On the left is shown the distribution for a minimum depth of 10% below the continuum, and on the right for a minimum depth of 3σ . Each bin of AI is 200 km s^{-1} wide. Note that the last bin includes all quasars of $AI \geq 5000 \text{ km s}^{-1}$.

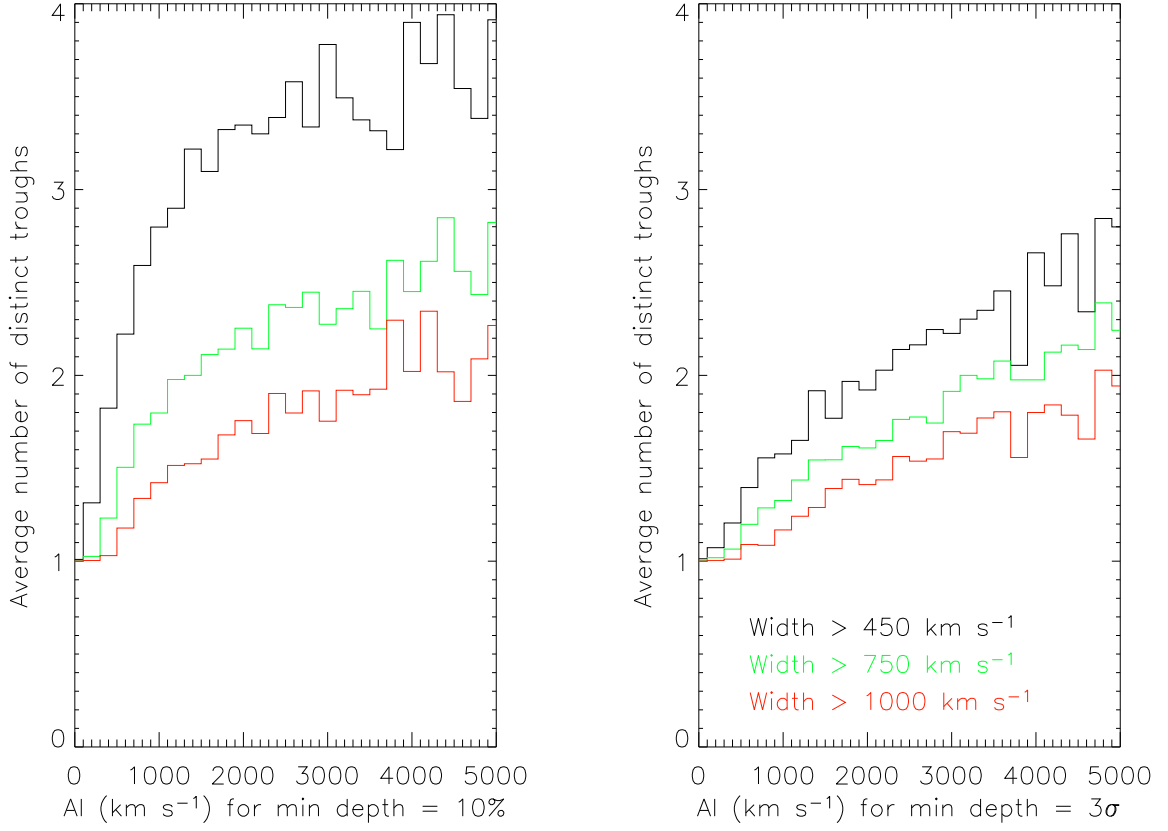


Fig. 4.— The average number of troughs in each BALQSO for given values of AI, calculated with different minimum depths and widths. A large number of troughs on average may indicate the identification of too many narrow troughs due to host absorption, intervening systems, and/or noise. Each bin of AI is 200 km s^{-1} wide.

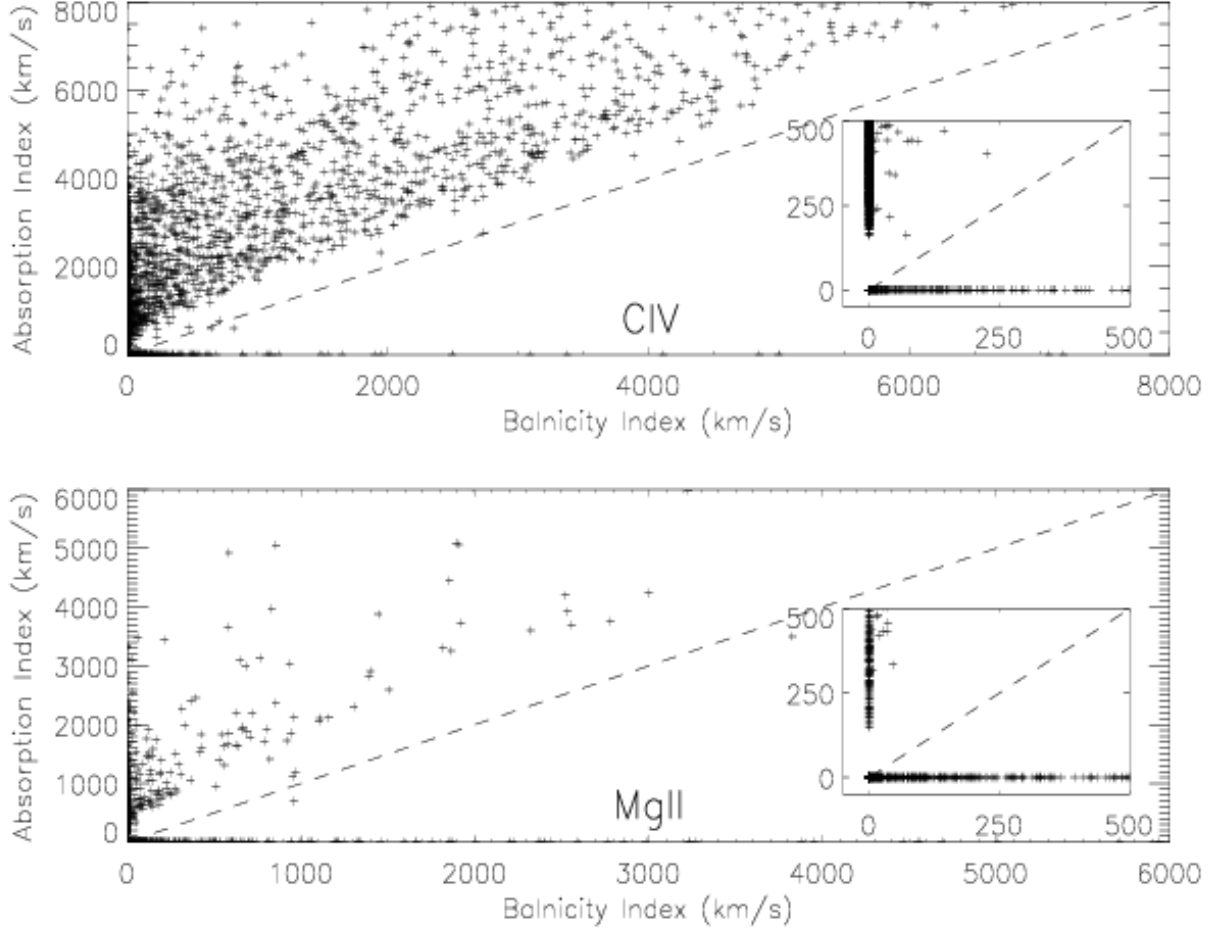


Fig. 5.— The absorption index vs. the balnicity index for the 5418 CIV BALQSOs (top) and 3032 MgII BALQSOs (bottom) in our catalog. Except for a handful of objects, the AI is greater than the BI because it includes all absorption, within the minimum depth and width. The AI is also significantly greater than the BI for many objects because it identifies narrower troughs and troughs near the zero velocity blueshift. The regions of low AI and BI are shown as insets. A few objects are identified to have $AI < BI$ because of our linear continuum restriction in the emission line region and our $\chi_0^2 \geq 10$ requirement for each trough in the AI calculation (see §4.3).

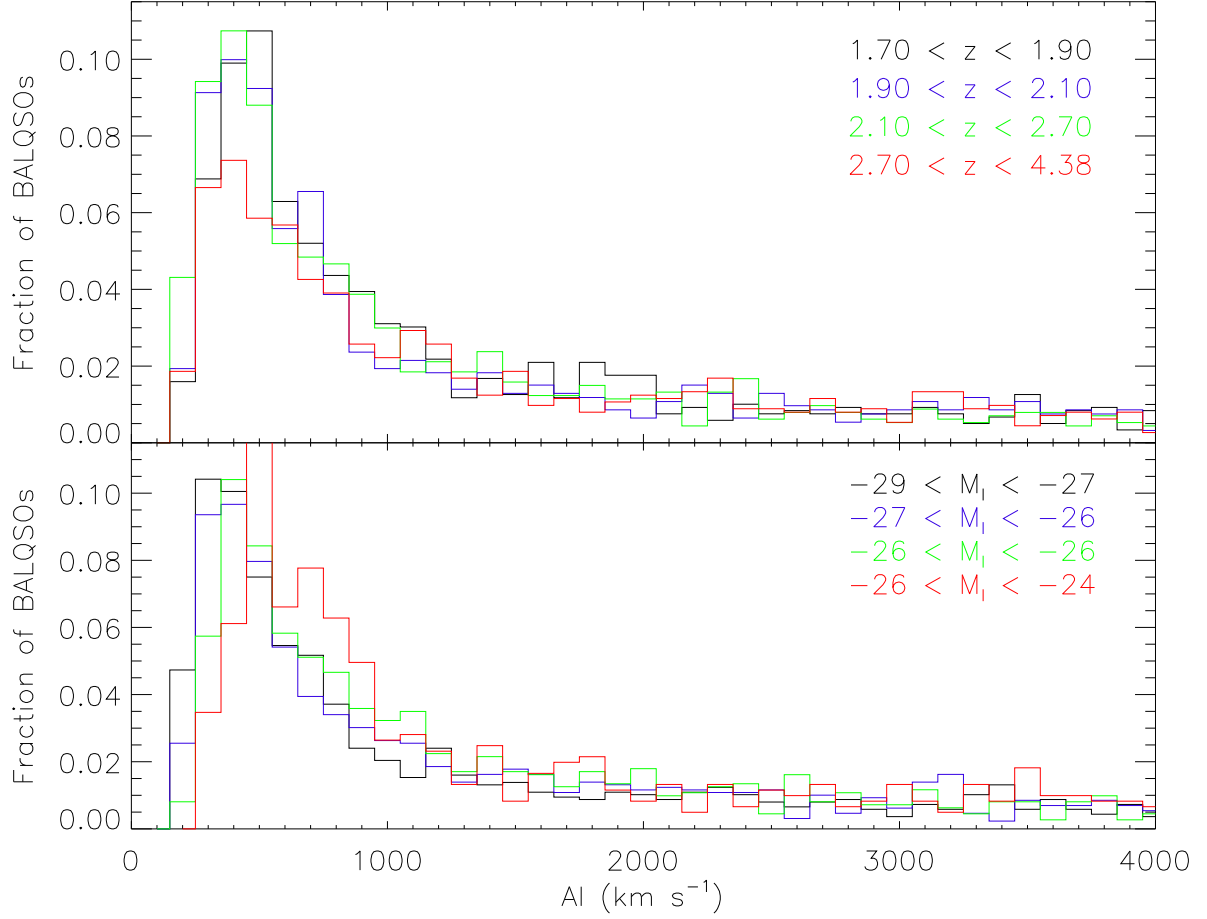


Fig. 6.— The distribution of computed AI values of the 5418 quasars in the redshift range $1.7 \leq z \leq 4.38$ with a nonzero AI (as defined in §4.3) in the CIV region. Each bin is 100 km s^{-1} wide. The peak in the distribution occurs at $\text{AI} \approx 400 \text{ km s}^{-1}$. While there are a substantial number of objects with $\text{AI} \geq 4000 \text{ km s}^{-1}$, they are evenly distributed and there are no interesting features in the distribution beyond the displayed range.

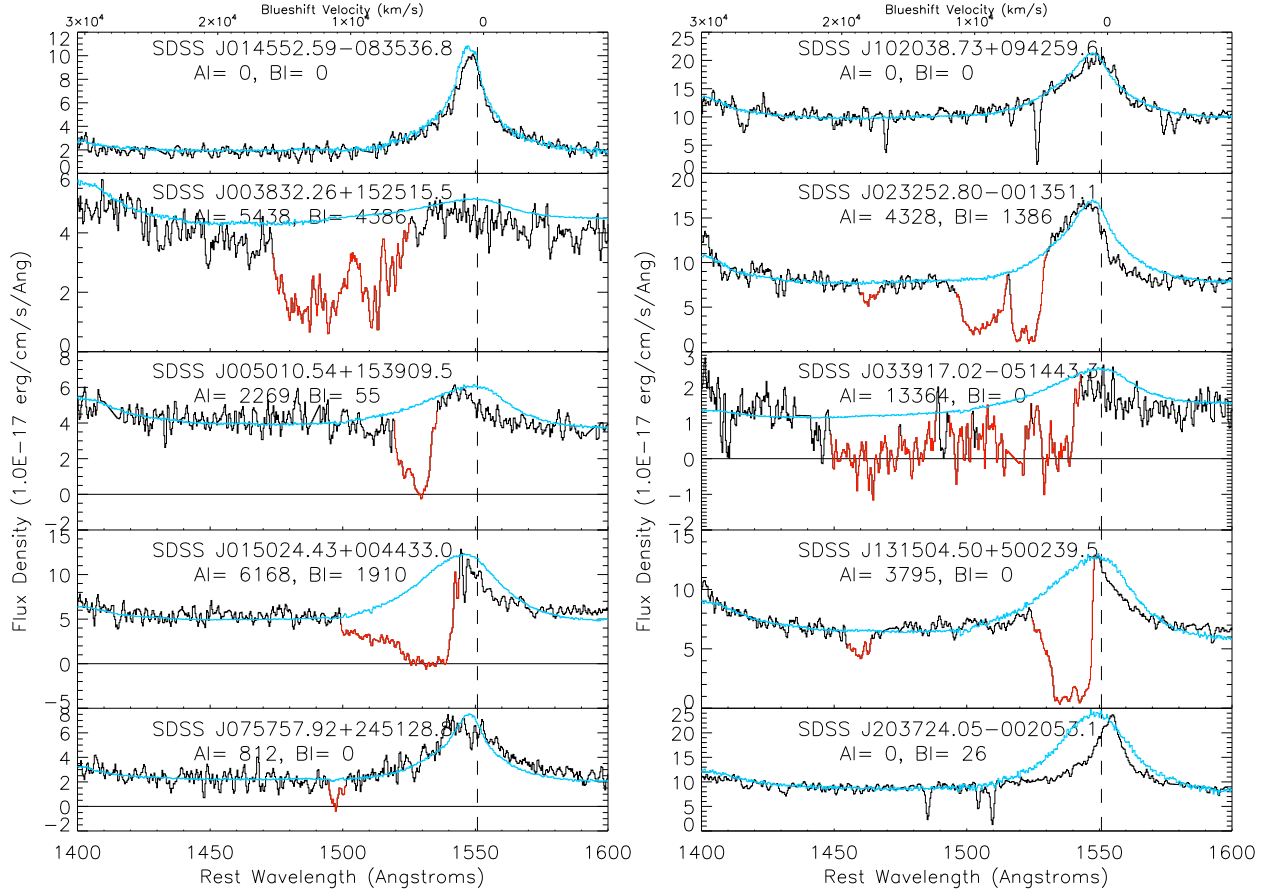


Fig. 7.— Two non-BALQSO spectra, seven example BALQSOs, and one object with $BI > 0$ and $AI = 0$ plotted in the region 1400-1570 Å. These objects were chosen as examples to show fitted continua in the CIV region and to show the differences between the AI and BI. All ten are discussed individually in §5.1. All spectra are smoothed by 3 pixels (roughly the SDSS resolution element). Spectral regions identified as BAL troughs (according to the AI definition) are designated in red.

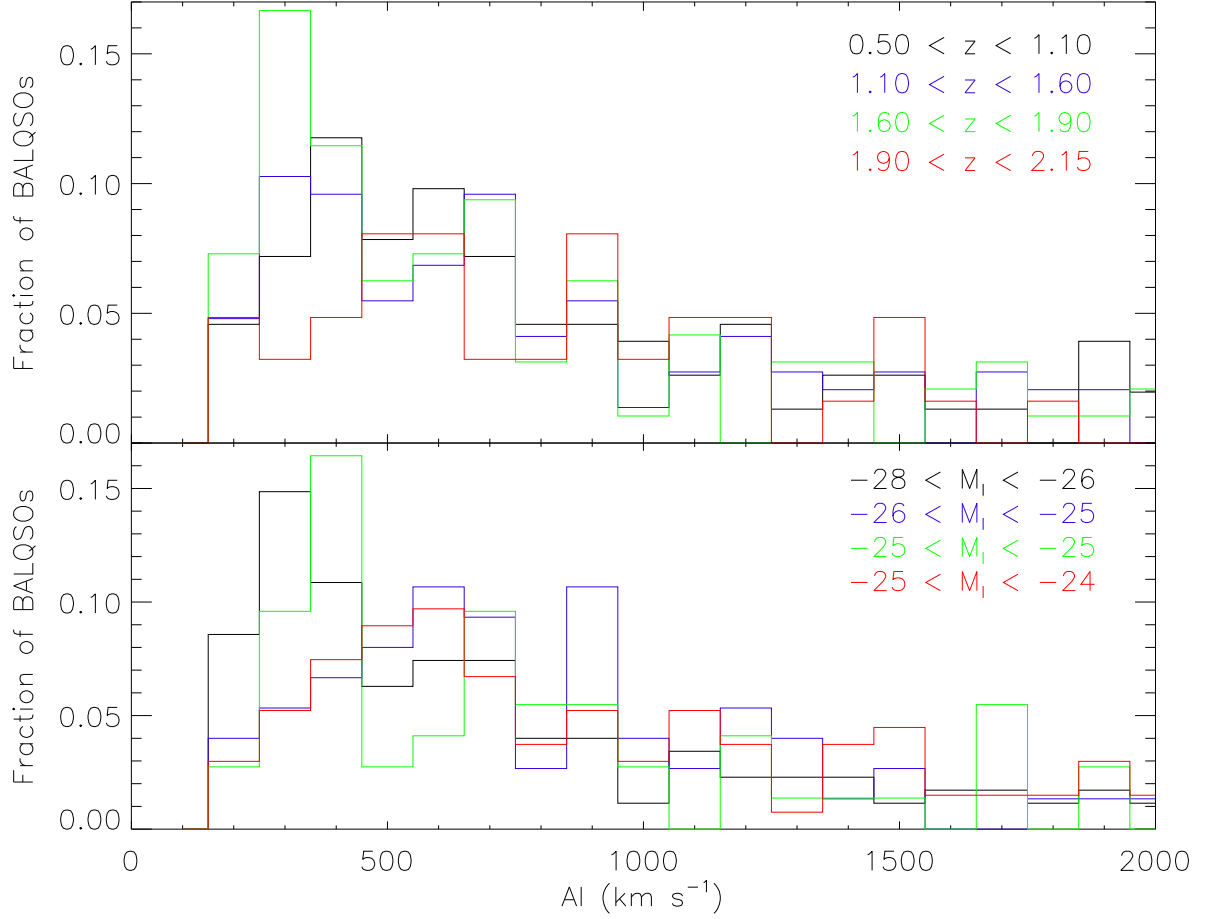


Fig. 8.— The AI distributions of quasars with nonzero MgII AI in different redshift and luminosity bins. Each bin is 50 km s^{-1} wide. The distribution peaks at about $\text{AI} \approx 350 \text{ km s}^{-1}$, and only a few quasars have $\text{AI} > 2000 \text{ km s}^{-1}$ in the MgII region.

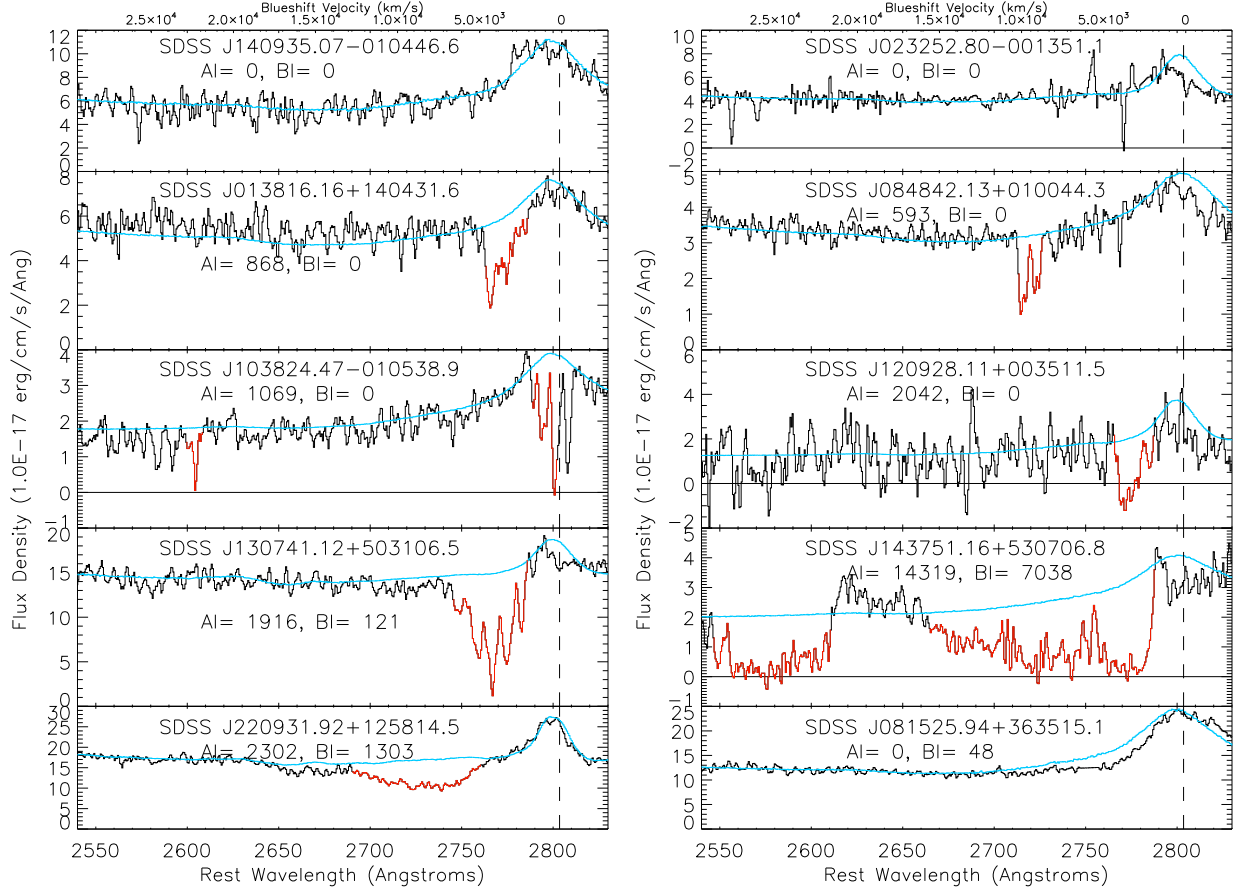


Fig. 9.— Two non-LoBALs, seven LoBAL spectra, and one object with $BI > 0$ and $AI = 0$ plotted in the region 2570-2830 Å. These objects were chosen as examples to illustrate our definition of LoBALs and the differences between the AI and BI. They are discussed individually in §5.2. Spectral regions identified as BAL troughs (according to the AI definition) are designated in red.

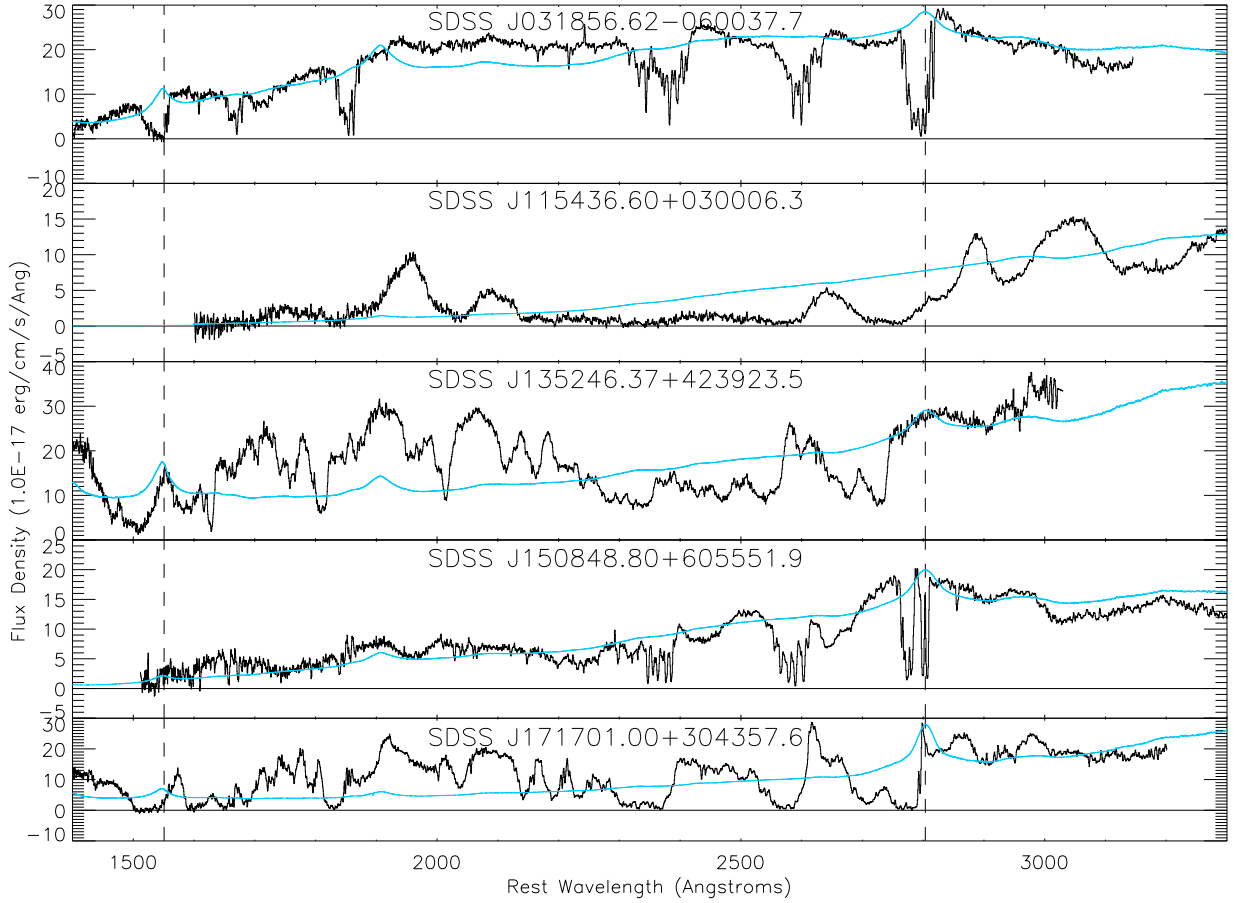


Fig. 10.— Five FeLoBALs at rest frame wavelengths 1400-3300 \AA , with the centers of CIV and MgII emission shown as vertical dashed lines. Overplotted in blue on each spectrum is the MgII continuum fit (quasars with $1.7 \leq z \leq 2.15$ also have a separate CIV continuum fit). All FeLoBALs in our catalog were identified by visual inspection. All five of these FeLoBALs exhibit strong absorption throughout their spectra, making continuum fitting and automatic identification extremely challenging.

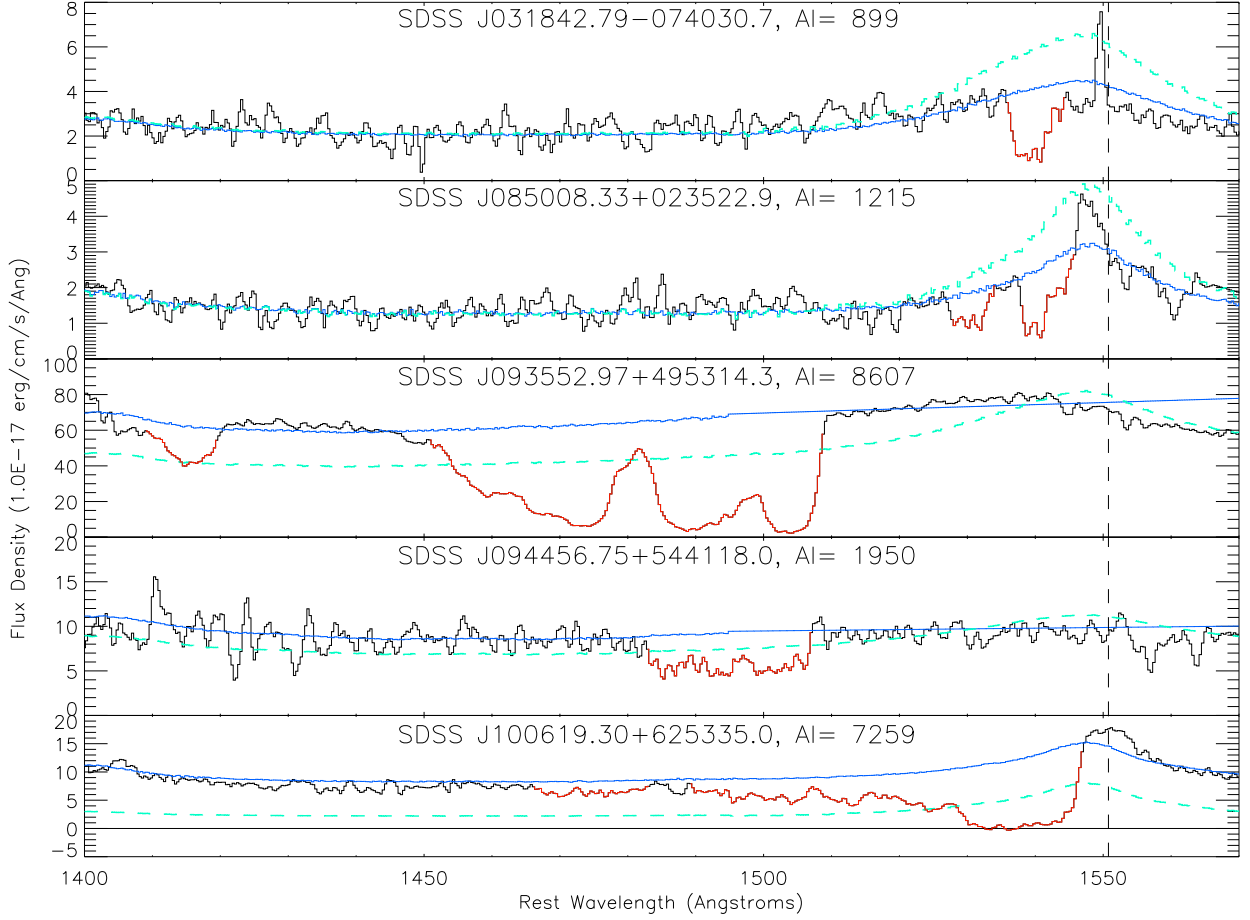


Fig. 11.— Five quasars with manually adjusted best-fit templates. The original automatically determined best-fit template is shown as the dashed teal line and the manually adjusted best-fit template is shown as the blue line. Each spectrum and its manually adjusted template is described in §5.4.

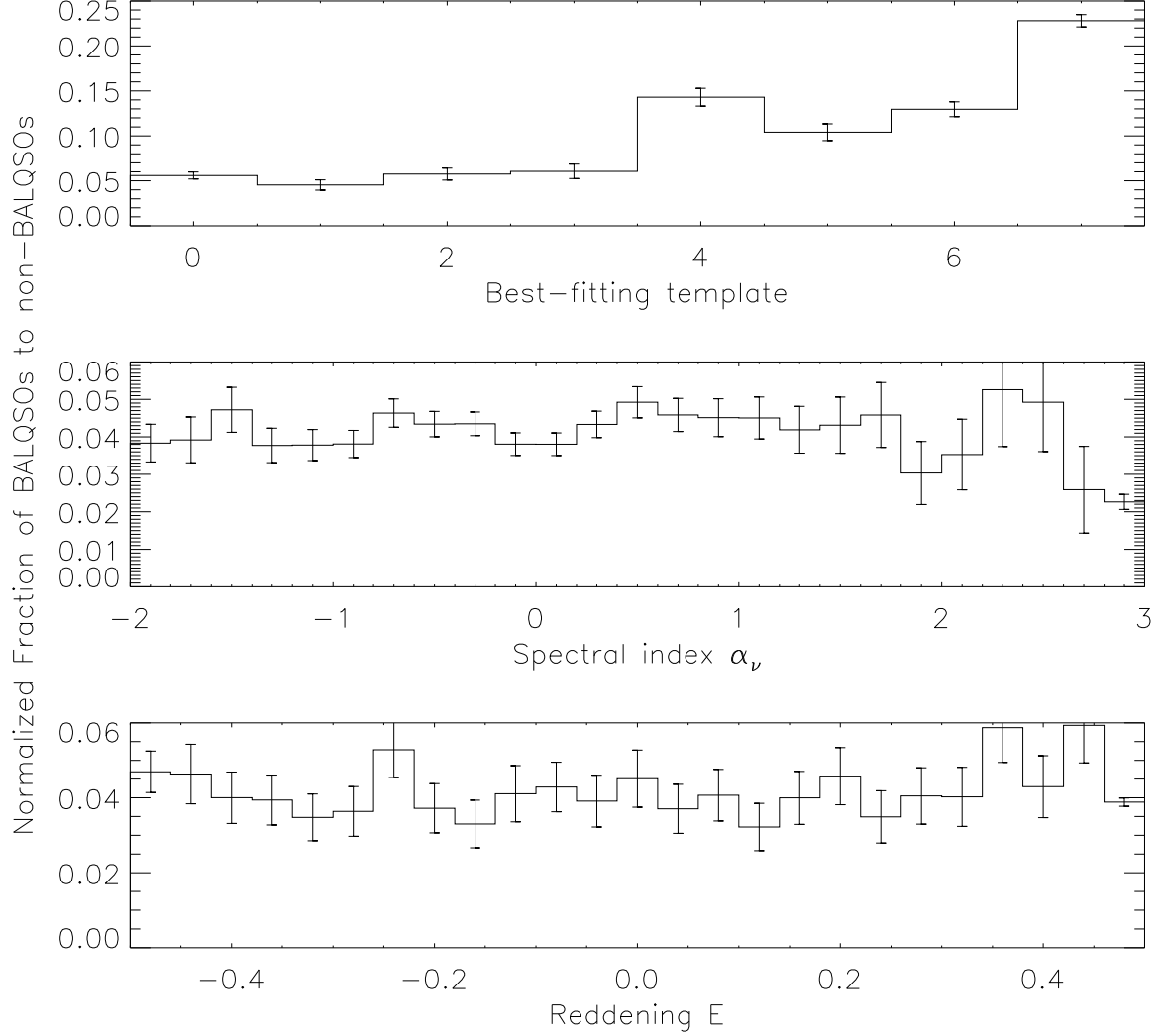


Fig. 12.— Histograms of the normalized ratio of C IV BALQSOs to non-BALQSOs with best template fit, spectral index, and reddening. Templates 0-3 are in the less luminous bin and 3 and 7 are the widest line width bins. Higher values of the spectral index represent bluer continua, while higher values of the reddening represent redder continua. We include only BALQSOs with spectral SNR > 9 in order to remove any luminosity effects on the fitting, since BALQSOs with low signal-to-noise may only be identified if they are more luminous. The preference for BALQSOs to be fit by the more luminous and widest line width template is probably a physical effect.

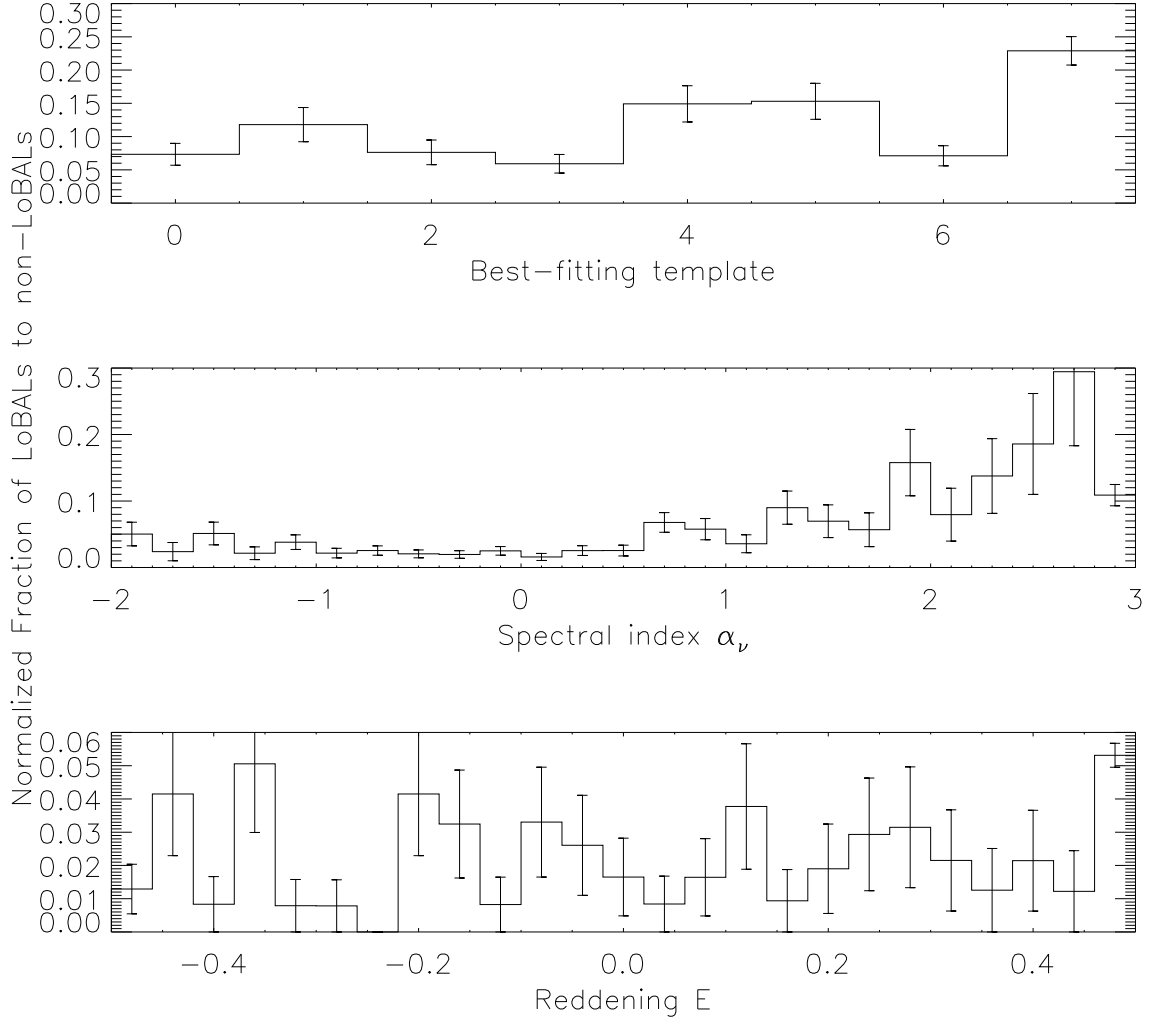


Fig. 13.— Histograms of the normalized ratio of MgII LoBALs to non-LoBALs with best template fit, spectral index, and reddening. Templates 0-3 are in the less luminous bin and 3 and 7 are the widest line width bins. We include only LoBALs with spectral SNR > 9 in order to remove any luminosity effects on the fitting. As with BALQSOs, the preference to be fit by the more luminous and widest line width template is probably a physical effect. The preference for fitting by bluer spectral indices may be a bias since fitting the possibly highly absorbed LoBAL continua may prefer more extreme fits.

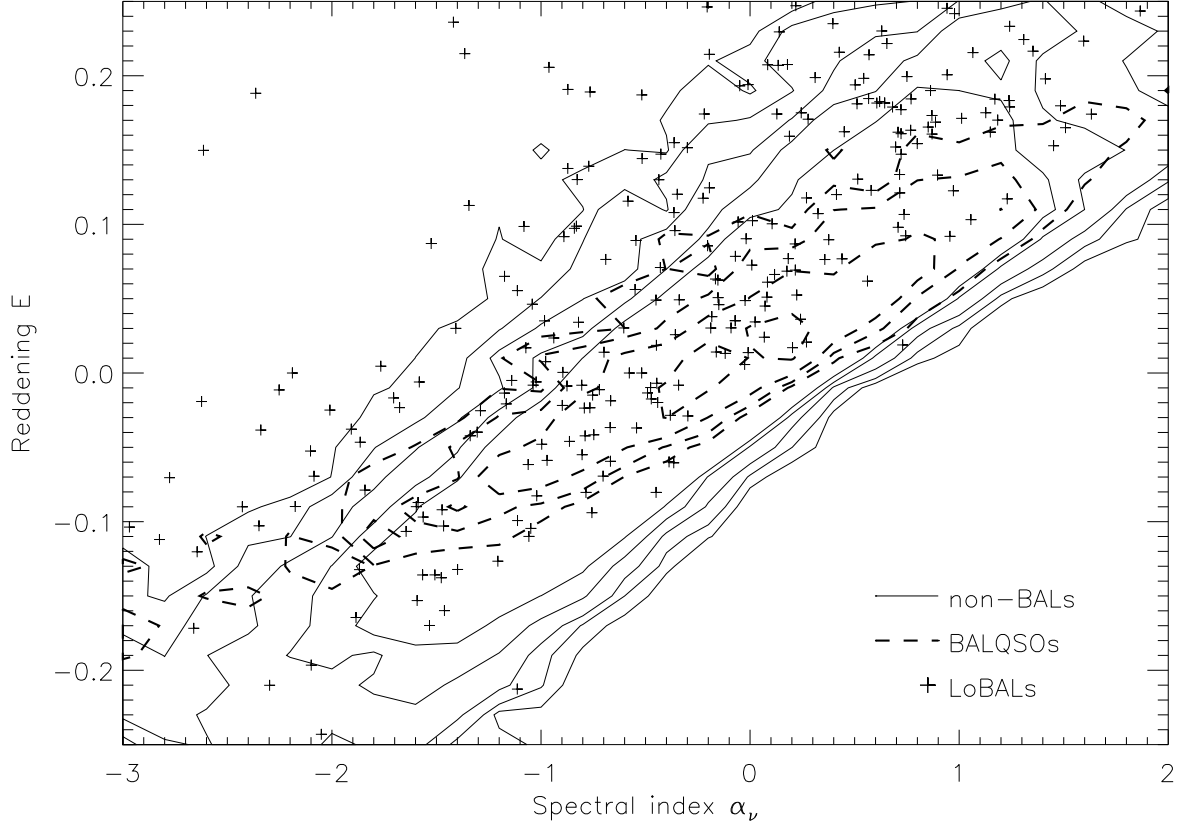


Fig. 14.— Reddening versus spectral index for BALQSOs and non-BALQSOs. The solid contours show the density of non-BALQSOs, the dashed contours show the density of BALQSOs, and LoBALs are overplotted as symbols. The spectral index and reddening are highly degenerate over the limited wavelength baseline of the SDSS spectra, so the formal ‘best-fit’ values are often unphysical. Despite this degeneracy, all three distributions are statistically different from each other at high significance, in the sense that BALQSOs (and especially LoBALs) are more reddened than non-BALQSOs.